FREQUENCY DEPENDENT SEISMIC REFLECTION ANALYSIS: A PATH TO NEW DIRECT HYDROCARBON INDICATORS FOR DEEP WATER RESERVOIRS

A Dissertation

by

SEUNG CHUL YOO

Submitted to the Office of Graduate Studies of
Texas A&M University
in partial fulfillment of the requirements for the degree of

DOCTOR OF PHILOSOPHY

August 2007

Major Subject: Geophysics

FREQUENCY DEPENDENT SEISMIC REFLECTION ANALYSIS: A PATH TO NEW DIRECT HYDROCARBON INDICATORS FOR DEEP WATER RESERVOIRS

A Dissertation

by

SEUNG CHUL YOO

Submitted to the Office of Graduate Studies of
Texas A&M University
in partial fulfillment of the requirements for the degree of

DOCTOR OF PHILOSOPHY

Approved by:

Chair of Committee,	Richard L. Gibson Jr.
Committee Members,	Daren Cline
	Akhil Datta-Gupta
	John R. Hopper
	Joel Watkins
Head of Department,	John H. Spang

August 2007

Major Subject: Geophysics

ABSTRACT

Frequency Dependent Seismic Reflection Analysis:
A Path to New Direct Hydrocarbon Indicators
for Deep Water Reservoirs. (August 2007)
Seung Chul Yoo, B.S., Korea University;
M.S., Pennsylvania State University
Chair of Advisory Committee: Dr. Richard L. Gibson Jr.

To better study frequency related effects such as attenuation and tuning, we developed a frequency dependent seismic reflection analysis. Comprehensive tests on full waveform synthetics and observations from the Teal South ocean bottom seismic (OBS) data set confirmed that normal moveout (NMO) stretch could distort both frequency and amplitude information severely in shallow events and far offset traces. In synthetic tests, our algorithm recovered amplitude and frequency information accurately. This simple but robust target oriented NMO stretch correction scheme can be used on top of an existing seismic processing flow for further analyses. By combining the NMO stretch correction, spectral decomposition, and crossplots of amplitude versus offset (AVO) attributes, we tested the frequency dependent workflow over Teal south and Ursa field data sets for improved reservoir characterization. As expected from NMO stretch characteristics, low frequencies have been less affected while mid and high frequency ranges were affected considerably. In seismic attribute analysis, the AVO crossplots from spectrally decomposed prestack data confirmed the improved accuracy and effectiveness of our workflow in mid and high frequency regions. To overcome poor spectral decomposition results due to low signal to noise ratio (S/N) in the Teal South application, we also implemented a substack scheme that stacks adjacent traces to increase S/N ratio while reducing the amount of data to process and increasing the accuracy of the spectral decomposition step. Synthetic tests verified the effectiveness of this additional step. An application to the Ursa, Gulf of Mexico, deep water data set showed significant improvement in high frequency data while correcting biased low frequency information.

To my parents

ACKNOWLEDGMENTS

First of all, I cannot thank my advisor, Dr. Richard Gibson Jr. enough for his guidance during my stay here at Texas A&M University. Without any exaggeration, he is one of the best advisors a student could ever have. Whenever I was in need, he was there. Moreover, it was my great honor and pleasure to have excellent committee members. Without their classes and advice on my research problems, I might have had stayed here longer. Drs. Cline, Datta-Guptta, Watkins offered me the best classes in statistics, geostastics, and geophysics respectively, while Dr. Hopper gave me excellent insights on amplitude preserving seismic processing and data analysis. Two other professors, Dr. Han and Dr. Batzle, helped me a lot in understanding rock physics through the joint project on seismic saturation.

I cannot forget to mention many friends in our research lab (Sung, Jin, Costas, John, Hung-Liang, Pablo, Chad, Ravi, Hoa). I really enjoyed my journey with them and learned a lot from them. My special thanks go to Woodong who helped me in many ways for the last several months. Most of all, I thank TGS-NOPEC Geophysical Company for providing a field data set. I also thank Paradigm Geophysical for the AVO inversion software (probe) and Landmark for seismic processing software (ProMAX), which were very helpful tools in this disseration.

Last but not least, my parents have been waiting for my graduation too long. I have to thank them and my wife and sons for their patience.

TABLE OF CONTENTS

Page

CHAPTER Page

LIST OF FIGURES

FIGURE Page

FIGURE Page

FIGURE Page

FIGURE Page

LIST OF TABLES

CHAPTER I

INTRODUCTION

The measurements of seismic reflection properties such as amplitudes have been used quite successfully for the detection of hydrocarbons. An important example is the method of amplitude variation with offset (AVO), which measures changes in reflection amplitude with angle of incidence or, equivalently, changes in distance between seismic source and receiver. This and other similar quantities are often referred to as "seismic attributes". On the other hand, the estimation of hydrocarbon saturation, especially from surface seismic data, is still a challenging task. For example, even the most robust direct hydrocarbon indicator (DHI) based on P-wave seismic amplitudes for Tertiary age sediments may result in a 10-30% fraction of dry holes due to low hydrocarbon saturation (O'Brien, 2004).

To solve this problem, we were motivated by recent rock physics models and field data studies suggesting frequency dependency of these seismic attributes. Previous researches were based on Biot's theory (Biot, 1956) to study fluid saturation within poroelastic layers with which can not explain observed attenuation. Batzle et al. (2001) measured velocities over broad frequency band and pointed out that the traditional Biot's theory would not appropriate under many conditions. Their observed dependence on pore fluid viscosity was consistent with local or squirt-flow theories. Han and Batzle (2002) elaborated on the importance of understanding of deep-water petrophysics while correcting misconceptions related to fizz water, which is a petroleum industry term describing brine with a small amount of dissolved gas. In more typical, shallow water exploration that has been the focus of the petroleum industry for a long time, this small amount of gas can change seismic velocities significantly. The changes in seismic reflection amplitudes can then be mistaken for an economic reservoir with a large volume of gas. However, their new measurement showed that water velocity change from dissolved gas were minimal at high pressure environments typical of deep water environments. More importantly, they

---

This dissertation follows the style and format of Geophysics.

proposed attenuation as a key attribute for the gas saturation evaluation. Throughout a frictional-viscous theoretical model, Goloshubin and Korneev (2000) illustrated a way to detect liquid saturated areas in a thin layer. Goloshubin and Daley (2001) and Goloshubin et al. (2002) suggested low frequency anomalies as one of the methods to detect and monitor hydrocarbons and processed the data while preserving low frequency content.

On the other hand, relatively old concepts of seismic low frequency effects revived through the advancement of computing powers. Low frequency effects (or shadows) is a phenomenon that shows up beneath amplitude anomaly, which is believed to be caused by high attenuation in gas filled reservoirs. Stronger amplitudes can be observed at low frequency data compared with at high frequency data below gas reservoir. Castagna et al. (2003) went through various field data examples on the detection of gas reservoirs, but could not completely explain the theoretical aspect of this phenomenon. In their continuous time-frequency analysis, they demonstrated that a much better time-frequency resolution has been achieved. More importantly, they pointed out that the tuning thickness concept became out of obsolete because any frequency ranges or single frequency could be studies resulting in more than a single tuning thickness. Ebrom (2004) listed many possible reasons for this effect while blaming processing artifacts such as NMO stretch as one of the reasons for low frequency effects. The framework of spectral decomposition can be found at Partyka et al. (1999) and many field data applications and case histories proves its usefulness (Burnett et al., 2003; Johann et al., 2003).

Based on these results, we hypothesize that frequency related effects can provide improved methods for detecting hydrocarbons and better insights on estimating saturation in deep water settings. One of the biggest challenges in testing this hypothesis is that rock and pore fluid properties in deep water environments are poorly understood (Han and Batzle, 2005; Han and Batzle, 2006) due to great amount of pressure. Moreover, with conventional rock physics models, it is particulary difficult to discriminate between low and high gas concentrations. A systematic approach combining rock property measurement and seismic and well log data analysis has to be used to solve this difficult problem (Batzle et al., 2002). From recent rock physics lab experiment, it was suggested that low gas saturation was normally correlated with high attenuation, which can considered as a frequency related effect.

To study the frequency related effects such as attenuation and tuning more ac-

curately, we need to develop a scheme that considers individual frequency component because different constructive or destructive interferences will occur in each frequency component. While we are interested in systematic changes of frequencies due to attenuation, other obscuring effects from wave propagation or processing artifacts will complicate frequency analysis. Thus, we first need to understand what roles rock properties, wave propagation phenomena, and processing artifacts play to change frequency information for a successful application of our algorithm.

As mentioned briefly before, one example of frequency related effects is attenuation (Q), which is becoming an important subsurface properties due to its sensitivity to fluid saturation (Han and Batzle, 2002). The study of attenuation is not an easy problem, because it might make seismic amplitude dependent on frequency along with wave propagation effects such as tuning. 1-D wave equation solution including attenuation coefficient can be written in terms of dislacement u as

$$u(x,t) = u_0 e^{i(kx-\omega t)}, \tag{1.1}$$

where x is distance, t time, u_0 an initial displacement at x=0, k wavenumber, ω temporal frequency. By setting the wave number complex such as

$$k = \frac{\omega}{c} + i\alpha, \tag{1.2}$$

where c is the phase velocity of propagating medium, allows a quantification of the effects of attenuation. Then, the displacement including the attenuation coefficient α becomes

$$u(x,t) = u_0 e^{-\alpha x} e^{i(kx-\omega t)}, \tag{1.3}$$

where

$$\alpha = \frac{\omega}{2cQ}. \tag{1.4}$$

If Q and c are independent of frequency, attenuation coefficient becomes the linear function of frequency. High frequency signals will be attenuated more. Experiments show that Q is strongly affected by fluid saturation and seismic frequency and frequency dependence of Q can be explained by attenuation mechanism (Aki and Richards, 1980). Also, processing artifacts such as normal moveout (NMO) stretch could distort the frequency and amplitude content significantly depending on reservoir depths and offset locations, which poses further challenges in solving the problem.

In our seismic analysis, we combine existing processing and analysis elements, such as NMO stretch correction, spectral decomposition, and AVO analysis. To correct NMO stretch, equations for the stretch ratio can be estimated, and this stretch ratio can be thought as a linear correction factor (Dunkin and Levin, 1973). AVO crossplots based on a three-term equation over reservoir models with different fluid content were analyzed after the removal of offset-dependent tuning (Swan, 1999). The NMO stretch could be corrected using a wavelet deconvolution (Castoro et al., 2001), but this might suppress measurable low frequency effects. This limitation can be relieved by using wavelet deconvolution using near offset traces (Lazaratos and Finn, 2004) as long as good quality near offset data is available.

Once we correct processing artifacts, data need to be decomposed into band of signals or each frequency slice. This spectral decomposition is the second element of our seismic workflow. The most popular way is based on windowed Fourier transforms. For detailed frequency analysis, we need more sophisticated time-frequency representations. The Gabor transform-like multifilter analysis technique pass each seismic trace into a group of Gaussian filters (Dziewonski et al., 1969). The wavelet matching scheme (Liu et al., 2004) found to be very useful in our analysis.

Our last element of seismic workflow is based on conventional AVO analysis technique. AVO is one of many direct hydrocarbon indicators (DHIs), which is a measurement suggesting the hydrocarbon accumulation. Ostrander first popularized AVO analysis as a direct hydrocarbon indicator using field data set (Ostrander, 1986). He showed that gas sand reflection coefficient could vary in a significantly anomalous way with increasing offset. Before his publication, there have been many theoretical works already, but only after Ostrander's work, people started using is as an exploration tool providing lithology information from seismic data. Zoeppritz (1919) solved for the reflection and transmission coefficients with respect to incident angle, densities, and elastic moduli, but this initial work provided complex equations without any substantial physical insights. Due to this reason, many approximations followed. Bortfeld (1961) linearized the Zoeppritz equation by assuming small changes in layer properties. Aki and Richards (1980) derived symmetrical equations in terms of density, P- and S-wave velocities. Shuey (1985) modified Aki and Richards' equation that simply describes the reflection coefficient (R) change in terms of normal

incidence reflectivity (NI) and AVO gradient (G).

$$R(\theta) = NI + Gsin^2\theta, \tag{1.5}$$

where θ represents an angle of incidence. But, like others, this technique does have some drawback. Due to large uncertainties of AVO analysis, it may not work in some cases resulting in mixed results (Houck, 1999; Sbar, 2000). In spite of the above drawbacks, many successful hydrocarbon detection based on AVO has reported: Gas detection examples from North Sea (Wrolstad, 1986; Strudley, 1990) and offshore Gulf of Mexico (Ostrander, 1986; Rutherford and Williams, 1989). Also, under certain conditions, successful oil detection using AVO technique does exist (Gassaway, 1984; Chiburis, 1987). Lin and Phair (1993) took into account tuning effect in their AVO study. Li et al. (2007) went through practical issues with AVO modeling to enhance reservoir characterization and to reduce risks. Stovas et al. (2006) performed AVO attributes inversion for finely layered reservoirs approximating a turbidite reservoir by a stack of thin shale-sand layers. Liu et al. (2006) used spectral decomposition for AVO analysis using four well data in the west of Shetland. Gomez and Tatham (2007) used the complete Zoeppritz equation and showed that additional information from P-SV and SH-SH AVO information is important in understanding partial gas saturation problem.

Our AVO inversion tool that inverts seismic data measurement for two AVO attributes is based on the above Shuey's equation which is known to be valid up to 30 degrees of incident angles. Most important point in conventional AVO analysis is that it is not considering any frequency dependent amplitude, attenuation, nor tuning. The reason why we need to look further frequency dependency of amplitudes will be illustrated in a simple synthetic example in the next section.

1.1 Why frequency dependent AVO analysis?

The following simple synthetic computations illustrate why we need a new approach to generate frequency dependent attributes while clarifying the relationships among the three frequency related effects mentioned before. Frequency information works as a link between attenuation and seismic data. Attenuation derived from seismic data, in turn, can be used as another link to seismic saturation combined with rock physics study and well log analysis.

Full waveform synthetics and their magnitude spectra from a thin layer model have been computed (Figure 1.1). In this kind of modeling, the ratio between layer thickness and wavelength is important and wavelength is a function of velocity and frequency. Central frequency of 40 Hz, medium velocity 2000 m/s, layer thickness of 30 m have been used, leading to a thickness/wavelengh ratio of 0.6. Meanwhile, NMO correction is a linear operation that makes all traces to zero offset ones assuming flat earth. For example, we can see hyperbolic moveout in our synthetics before NMO correction(Figure 1.1.a). After NMO correction, signals from each trace are aligned at zero offset time (Figure 1.1.b). Here, we wanted to model wider and stronger tails and to study adverse effects on frequency by NMO stretch and tuning, Wave propagation effect (tuning), processing artifact (NMO stretch), and rock property (Q, what we want) can change the frequency content of signals into different directions. The NMO stretch lowers frequency contents with increasing offsets (compare Figure 1.1.e and Figure 1.1.f or Figure 1.1.g and Figure 1.1.h), while tuning could increase the amplitude with offset due to the constructive interferences by the reflections from the top and bottom of the thin layer. Q, by definition, decreases amplitude of high frequencies more while low frequencies are being further emphasized. But, as shown in Figure 1.1.h, the combination of the above three frequency related phenomena could counter-intuitively increase the amplitude with offset in the case of Q inclusion, which could be used as an evidence of low attenuation (Figure 1.1.g and h).

1.2 Overview of dissertation

The goal of this dissertation is to develop a robust workflow for the study of frequency dependent attributes while overcoming the following technical challenges:

- Conventional processing flows before AVO analysis do not consider seriously the conservation of frequency content. For example, wavelet deconvolution that is routinely applied to seismic data could suppress important low frequency information.
- Processing artifacts such as NMO stretch can also distort frequency content, which pose further challenges in frequency analysis.
- Conventional AVO analyses are based on full bandwidth data in which interferences among frequencies exist.

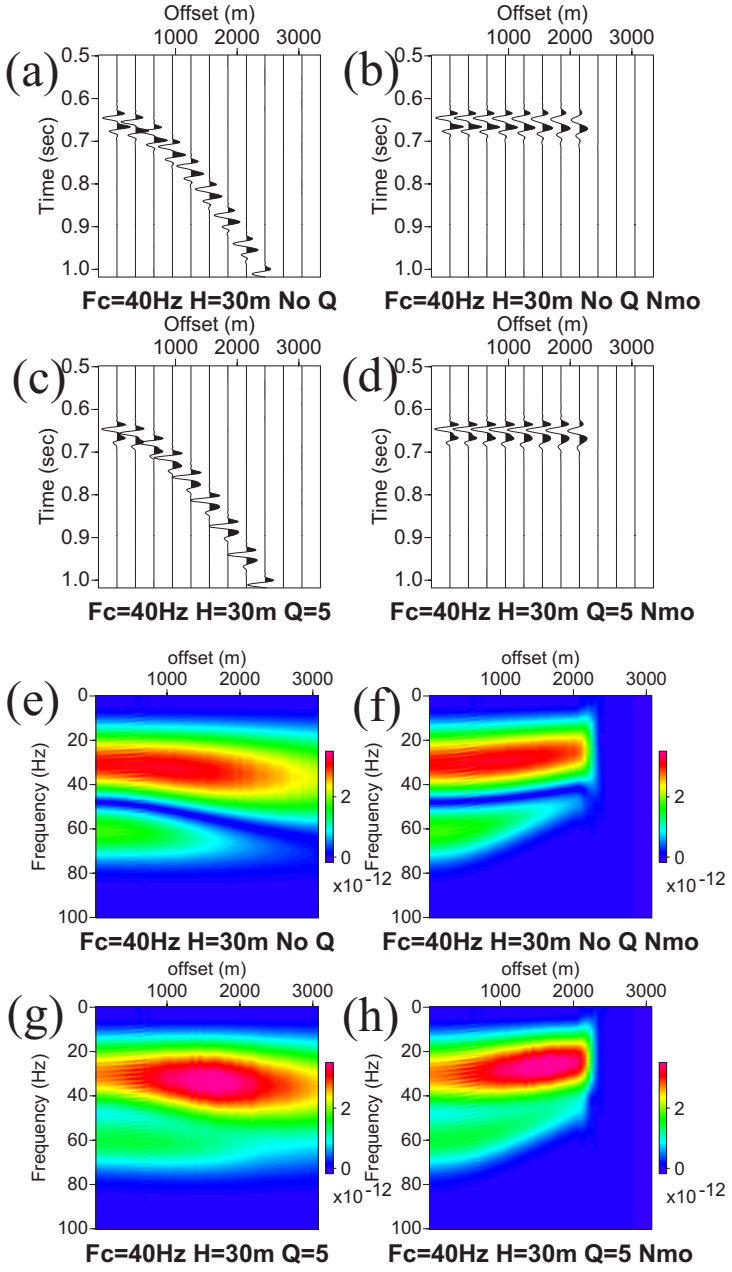

Fig. 1.1. Shot gathers (a-d) before NMO and after NMO and their magnitude spectra (e-h). The model in the first row does not include Q in the thin layer, while the model for second row includes Q in the thin layer. All other parameters were same except the inclusion of strong attenuation in the thin layer. Corresponding magnitude spectra are shown in the below figures: NMO stretching lowers frequency contents more with increasing offsets, while tuning could increase amplitude further with increasing offset due to the constructive interferences.

To achieve our goal, among three frequency related effects which are NMO stretch, tuning, and attenuation, we remove the processing artifact (NMO stretch), decompose signal into frequency slices, and apply conventional AVO analysis. To verify the effectiveness of our new algorithm, we used various synthetic data (Chapter II) and two field data sets (Chapters III and IV). Characteristics of available data sets and their objectives are summarized in Table 1.1.

1.2.1 Synthetic test of NMO stretch correction

In Chapter II, we test a NMO stretch correction scheme based on the shift of Fourier components by the stretch ratio. After detailed observations from the field data set, we identified that NMO stretch is the first order problem to be resolved for accurate AVO analysis. Through synthetic seismogram computations, we verify the effectiveness of our algorithm. We start from a very simple model (layer over half space), then apply this algorithm over multi-layered model while numerically verifying the accuracy of our approach. This correction successfully restored both frequency and amplitude information with great accuracy, which enabled more precise AVO analysis.

1.2.2 Field data test with shallow water reservoir

In Chapter III, we demonstrate that this simple but robust target oriented NMO stretch correction scheme can be used on top of an existing seismic processing flow for further analyses using Teal South (shallow water GOM) field data. Other than going back to the beginning of seismic processing flow, this can be applied to many existing data after NMO. Despite of suboptimal data condition of the field data set, our workflow shows significant improvement on high frequency data. After the stretch correction, we could observe systematic increases mainly in magnitudes of gradient attributes with better separations in crossplots, which enables us to detect hydrocarbons better. At the end, we compute synthetics from a model based on well log information to learn what to expect from the later deep water field data application.

Table 1.1. Available data sets and their objectives.

Name	**Characteristic**	**Objectives**
Teal South (GOM)	1. Shallow water (80 m) 2. NMO corrected CMP gathers 3. Demultiple using PZ summation 4. Some reservoir info is known	1. Test target oriented NMO correction algorithm 2. Identify problems in applying the new workflow
Ursa (GOM)	1. Deep water (1000 m) 2. Unprocessed shot gathers 3. Moderate amount of noise (multiples) near target areas 4. Some reservoir info is known	1. Test effects of different multiple attenuation methods on AVO analysis 2. Build amplitude preserving time processing workflow analysis workflow to known reservoirs 3. Test the frequency dependent AVO

1.2.3 Robust stretch correction algorithm with deep water reservoir

In Chapter IV, we carefully process the Ursa (deep water, GOM) field data set to preserve amplitude and frequency information. We use move-out based method for demultiple (radon method) and prestack time migration equivalent process (NMO + DMO + FK migration) for imaging. We implement a substack scheme that stacks adjacent traces to increase S/N ratio because poor spectral decomposition results was caused by low S/N ratio in our previous Teal South application. Synthetic tests verified the effectiveness of this additional step and an application to a deep water data set showed significant improvement in high frequency data while correcting biased low frequency information.

CHAPTER II

SYNTHETIC TEST OF FREQUENCY DEPENDENT AVO WORKFLOW

2.1 Introduction and summary

Most studies on AVO analysis are based on broadband data and neglect the frequency dependence of amplitudes and other seismic measurements. It is crucial to study a single frequency for better undertanding frequency related effects such as tuning or attenuation. This motivates us to develop a scheme that considers each individual frequency component, because different constructive or destructive interferences may occur in each frequency component. Such variations can provide additional constraints on reservoir structure or material properties.

In this chapter, starting from observations from the Teal South ocean bottom seismometer (OBS) data set, we test the target oriented NMO stretch correction scheme developed in the preceding chapter on various synthetic data sets. Our workflow for a detailed frequency study consists of NMO stretch correction, spectral decomposition, and crossplots of AVO attributes. After comprehensive tests of the preprocessing steps, we demonstrate that they allow much better recovery of correct amplitude and frequency information for amplitude analysis (both time-frequency spectral analysis and AVO). Also, a wavelet alignment scheme has been added for more accurate AVO inversion results. It should be noted that AVO attribute computation from commercial software (Probe from Paradigm) is performed at each time sample. Without proper alignment of waveforms using this scheme, significant amount of errors can be included in the AVO attribute inversion results. Using a multi-layered test model we demonstrate that this stretch restoration is a crucial step, especially for shallow and far offset traces. Based on well log data, we construct a model with two thin layers. It is noted that even thin upper layers with strong attenuation can affect reflections from lower layers.

2.2 Observations from field data set

A careful examination of waveforms reflected from a reservoir in the Gulf of Mexico demonstrates the problems that can arise in frequency dependent AVO analysis of legacy data that has not been carefully processed for this purpose (Figure 2.1). There are a couple of first order observations that are easily noticed. For example, the reflections from the 4500 ft reservoir become longer in period and larger in amplitude at larger offsets. This is especially noticeable in the black peaks at a reflection time of about 1.425 s. Even though these wider and stronger reflections may be indicative of attenuation and dispersion, they could also be simply a consequence source radiation pattern effects or multiple arrivals from other reflecting boundaries within the reservoir, including a free gas or rising oil-water contact.

Application of three overlapping band-pass filters to the CMP gathers from the field data allow a basic frequency-dependent AVO analysis. Specifically, we applied filters with the following trapezoidal filter parameters to the data:

1. Low frequency data: 4,8,28,25 Hz
2. Mid frequency data: 18,25,45,52 Hz
3. High frequency data: 35,40,60,90 Hz

Following the application of these three filters, the Probe software generated the AVO intercept and gradient measurements within the time window from 1.35 s to 1.60 s (see equation 1.5). After dividing the CMP gather into these three frequency regions, we defined a background anomaly (region outlined in red in Figure 2.2b) and excluded points falling within that range of intercept and gradient values in the cross-plots to pick anomalous regions (Figure 2.2d). This simplifies the identification of unusual values of AVO parameters that may correspond to reflections from productive reservoirs.

Figure 2.3 shows the resulting cross-plots of frequency-dependent AVO normal incidence and gradient parameters. At the low frequency data, we can observe anomalous region at upper right and lower left quadrants. At the mid frequency data where the dominant frequency was the same as the full bandwidth data, the anomaly pick was the most identical to that from the full bandwidth data. At high frequency data, we can notice that the anomaly in the crossplots is not easily distinguishable anymore. This effect is caused by NMO stretching artifacts where high frequency contents were

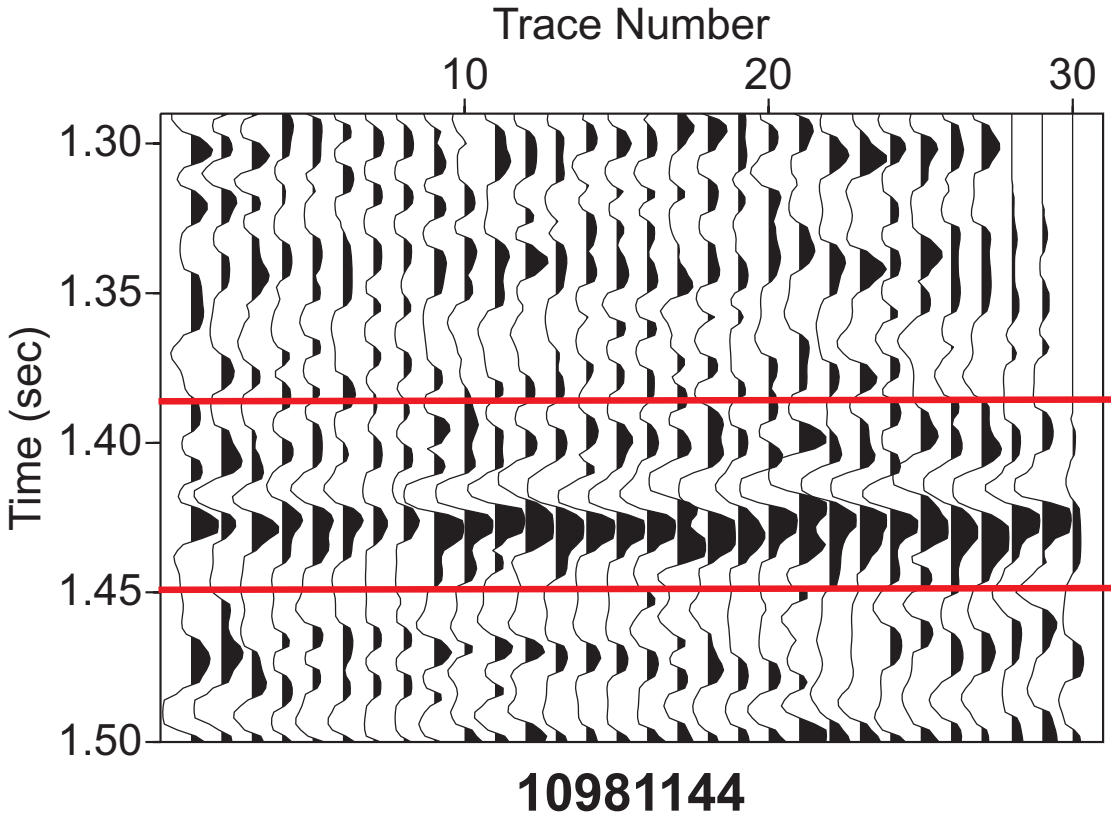

Fig. 2.1. A NMO corrected CMP (11981144) gather. The reflections from 4500 ft sand were windowed by red lines. The wider and stronger tails and stretched wavelets due to NMO stretching artifacts are easily noticeable. Weak reflections from the bottom of the reservoir arrive at 1.47 s.

affected more than the low frequency signal did. After the stretch correction, we will see more variations in the crossplot of AVO attributes from high frequency data after the stretch correction.

2.3 Methodology

NMO traveltime corrections lead to significant wavelet distortion, especially at large offsets, that hinders frequency-dependent analysis. Fortunately, it is possible to define a comparatively straightforward correction for these effects that can be applied to a specific target reflection. Specifically, Dunkin and Levin (1973) derived equations for stretch ratio and used it as a linear correction factor. Let t measure time in the data

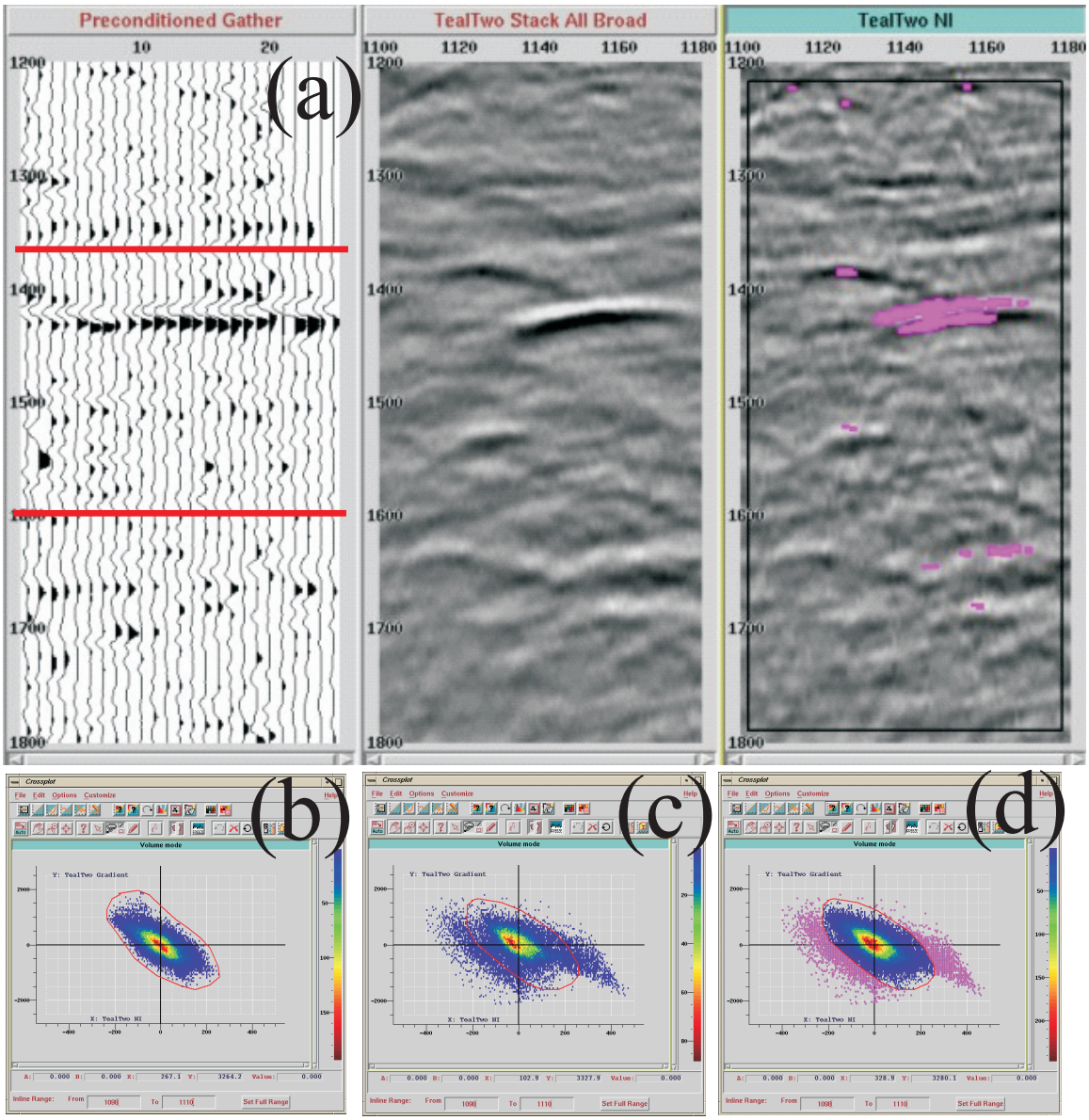

Fig. 2.2. Definition of background anomaly: (a) A CMP gather, stack, and NI attributes, (b) A crossplot of NI and gradient attributes from upper and lower data region in (a), leaving out the data between the red marker lines, (c) A crossplot of NI and gradient attributes from whole data region in (a), (d) A crossplot of NI and gradient attributes where the AVO anomaly is highlighted in pink.

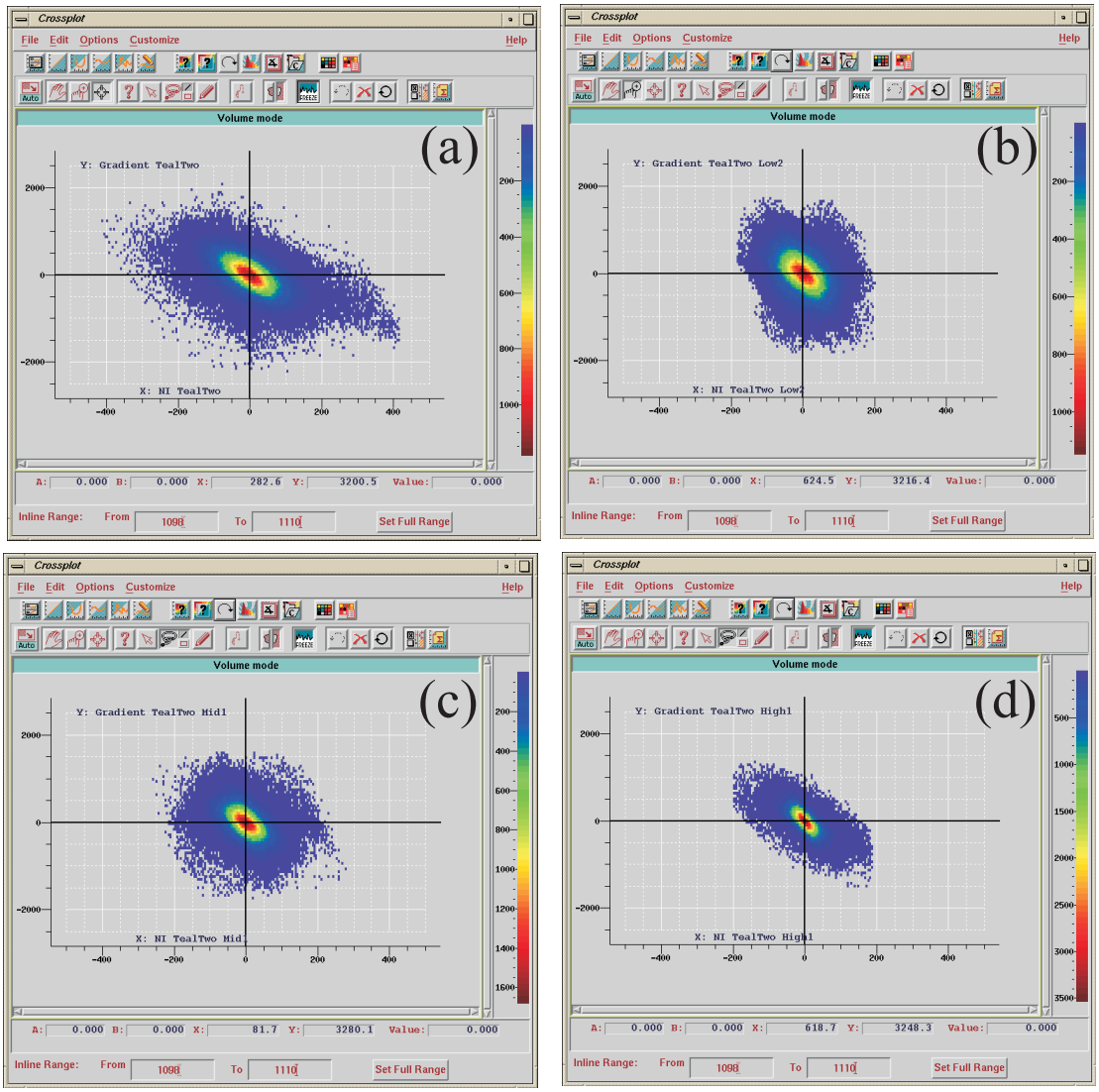

Fig. 2.3. Cross plots from band pass filtered data. Each cross plot from (a) Full bandwidth data, (b) Low frequency data (filter parameter: 4,8,28,25), (c) Mid frequency data (18,25,45,52),(d) High frequency data (filter parameter: 35,40,60,90). Notice the different shape on the cross-plots from low frequency data and hard-to-pick anomaly in high frequency data. x-axis represent normal incidence and y-axis gradient.

at some arbitrary receiver offset, and let t_0 be the time variable for the receiver at zero offset. After NMO, a wavelet on the receiver at abitrary offset that is centered at t_A is moved to time t_{0A} and is "stretched" to have longer period than the recorded signal. If you define $\tau = t - t_A$ and $\tau_0 = t_0 - t_{0A}$ as in Dunkin and Levin (1973), stretch ratio a can be defined as

$$\tau_0 = a\tau. \tag{2.1}$$

This leads the relationship between wavelets in time domain before, $g(\tau)$, and after NMO, $g_0(\tau_0)$, in the form

$$g_0(\tau_0) = g(\frac{\tau_0}{a}). \tag{2.2}$$

After the Fourier transform, the above equation becomes

$$\begin{aligned} \tilde{g}_0(f) &= \int_{-\infty}^{\infty} g_0(\tau_0) e^{-2\pi i f \tau_0} d\tau_0, \\ &= \int_{-\infty}^{\infty} g(\tau_0/a) e^{-2\pi i f \tau_0} d\tau_0, \\ &= \int_{-\infty}^{\infty} g(\tau) e^{-2\pi i f a \tau} a d\tau \end{aligned} \tag{2.3}$$

Therefore, we can relate the Fourier transforms of data before and after NMO as

$$\tilde{g}_0(f) = a\tilde{g}(af), \tag{2.4}$$

a simple and direct comparison showing that both period and amplitude of a wavelet will change.

Dunkin and Levin (1973) also show that this stretch ratio a can be estimated quite accurately as a function of offset, NMO velocity, derivative of NMO velocity with respect to the uncorrected travel time evaluated at corrected travel time, and scaled by the ratio between uncorrected travel time and corrected travel time:

$$a = \frac{t_A}{t_{0A}} \left(1 - \frac{X^2}{V^3 t_{0A}} \cdot \frac{V}{t_0}\Big|_{t_{0A}} \right)^{-1}, \tag{2.5}$$

where t_A is the uncorrected travel time, t_{0A} is the corrected travel time, X is the offset, and V is the NMO velocity.

A simple layer over half space model (Figure 2.4) has been used to generate synthetic seismograms and to illustrate how NMO stretch distorts frequency information. The top layer has P-wave velocity of 2600 m/s with density of 1.9 g/cm^3 and lower

half space 3200 m/s P-wave velocity with 2.4 g/cm^3 density. Source and receivers are located 6000 m above the layer interface while free surface effects were ignored. The corresponding synthetic seismograms were shown at Figure 2.5. Figure 2.6 shows the amplitude spectra from the 3000 m offset trace in Figure 2.5a. Before NMO correction (blue circle), the dominant frequency resides around 40 Hz. After NMO correction (red cross), we can clearly observe the shift of the dominant frequency to 30 Hz. By shifting the Fourier components using this stretch ratio amount, we can reverse the NMO stretch effect with correct frequency info. Specifically, we need a two step process:

1. Shift (or divide) the amplitude by stretch ratio (first stretch ratio a factor in the above equation in front of $\tilde{g}(af)$)

2. Shift the distorted each frequency amplitude to the right frequency location (stretch ratio a inside amplitude spectra g for each frequency component)

Note that the first shift (or spectral division) has been already applied in Figure 2.6 to emphasize the second spectral shift, which is more important for correct spectral information. Figure 2.7 shows the amplitude spectra after the shift. We can see that shifted spectrum (red cross) matches the original spectrum very well.

Though the frequency information has been restored correctly, the travel time of the wavelet maximum is unlikely to be aligned well from trace to trace, especially in noisy field data. Using crosscorrelation, we implement a conventional alignment scheme by first computing the amount of shift with respect to the near offset trace. By shifting the windowed data with computed delay, we finally get well aligned events resulting in more accurate amplitude measurement along specific time sample.

Next step is to decompose signal into the frequency of our interest, which provides a way of directly examining how amplitudes change with offset for various frequencies. We used wavelet matching algorithm by (Liu et al., 2004) and the major steps can be summarized as the following.

1. Calculate the complex seismic traces using Hilbert transform.

2. Calculate the envelope, instantaneous attributes of phase and frequency from the complex traces.

3. Find the time location of the maximum amplitude from the envelope.

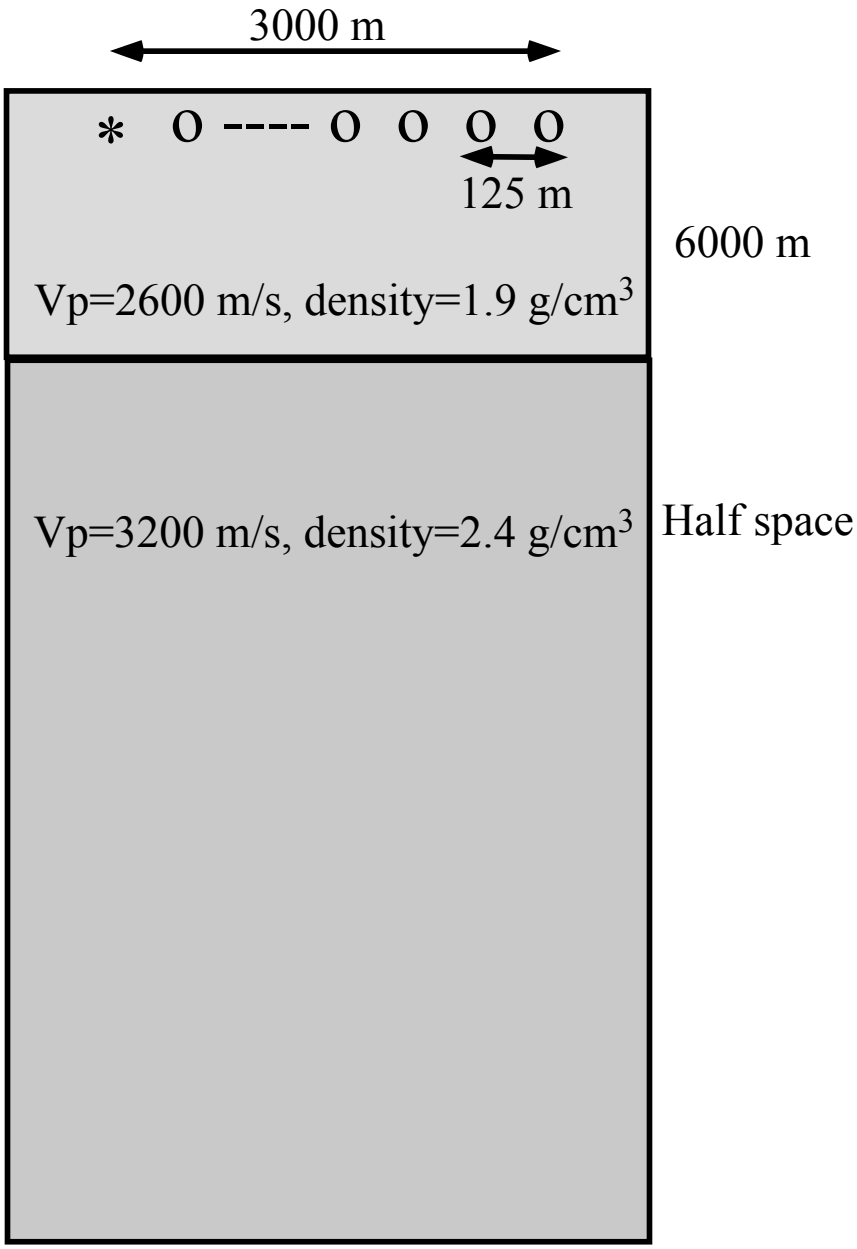

Fig. 2.4. Model parameters and acquisition geometry for a simple model. * represents source location and o receiver locations.

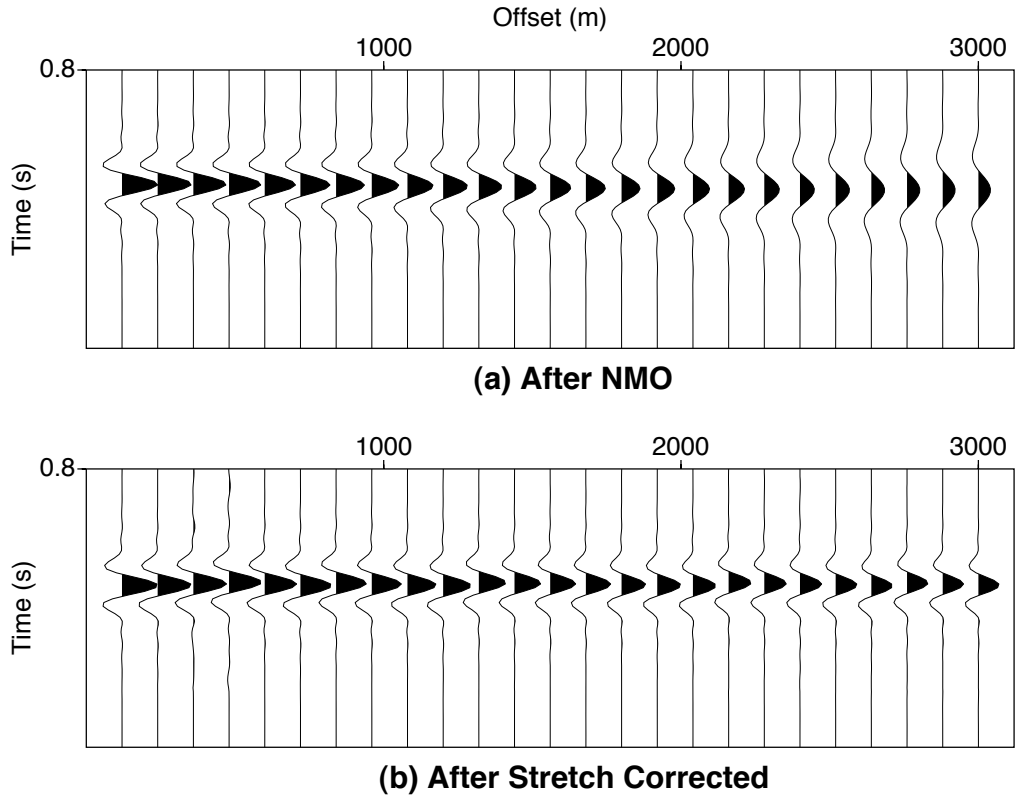

Fig. 2.5. Synthetic data from two half spaces model. (a) NMO corrected shot gather, (b) Stretch corrected shot gather. Notice wider wavelets with increasing offset after NMO.

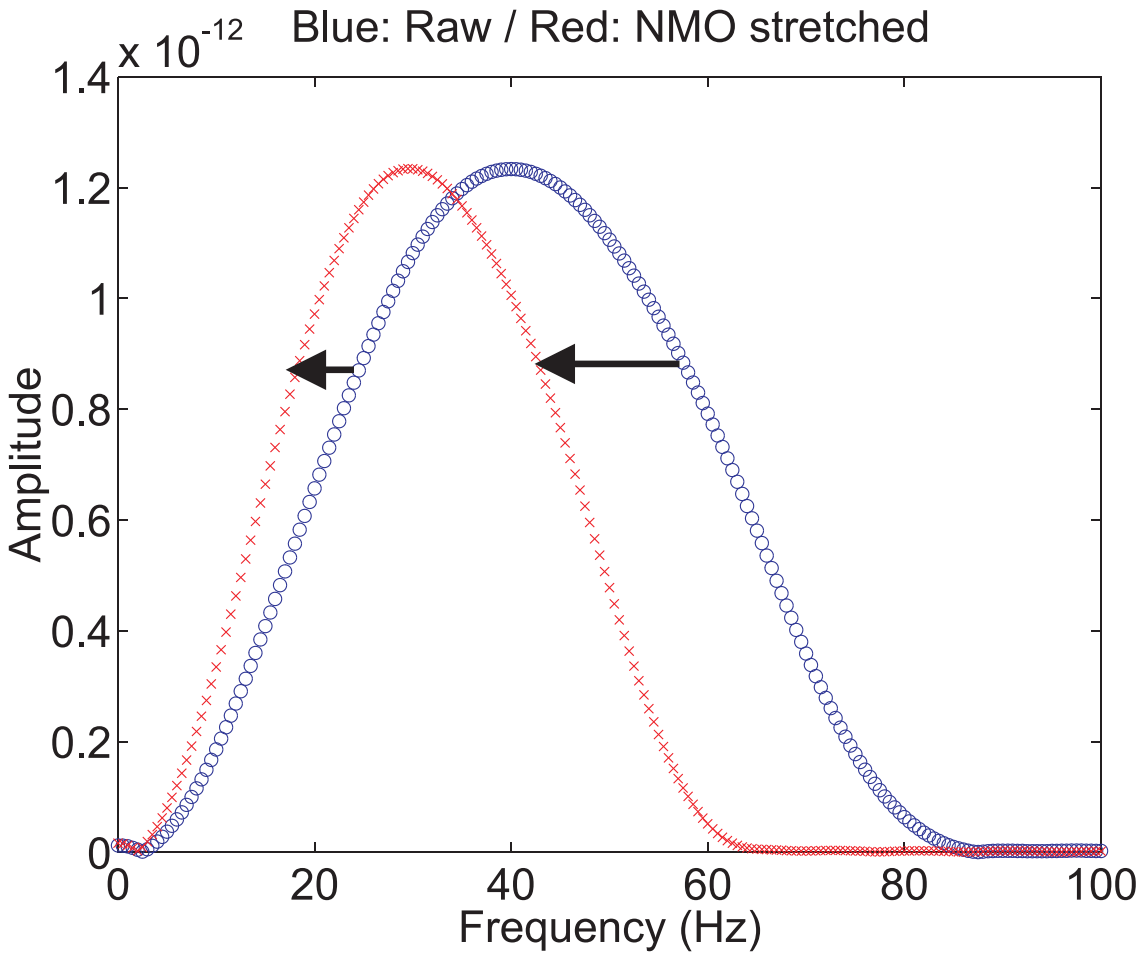

Fig. 2.6. Amplitude spectra before (blue circle) and after (red cross) NMO correction. Notice the shift of dominant frequency change due to NMO stretch.

4. Calculate dominant frequency and phase angle of complex Ricker wavelet by using instantaneous frequency and instantaneous phase.

5. Subtract the real part of complex Ricker wavelet from real seismic trace until certain threshold is meet.

6. Collect those subtracted Ricker wavelets which become the time frequency representation of the signal.

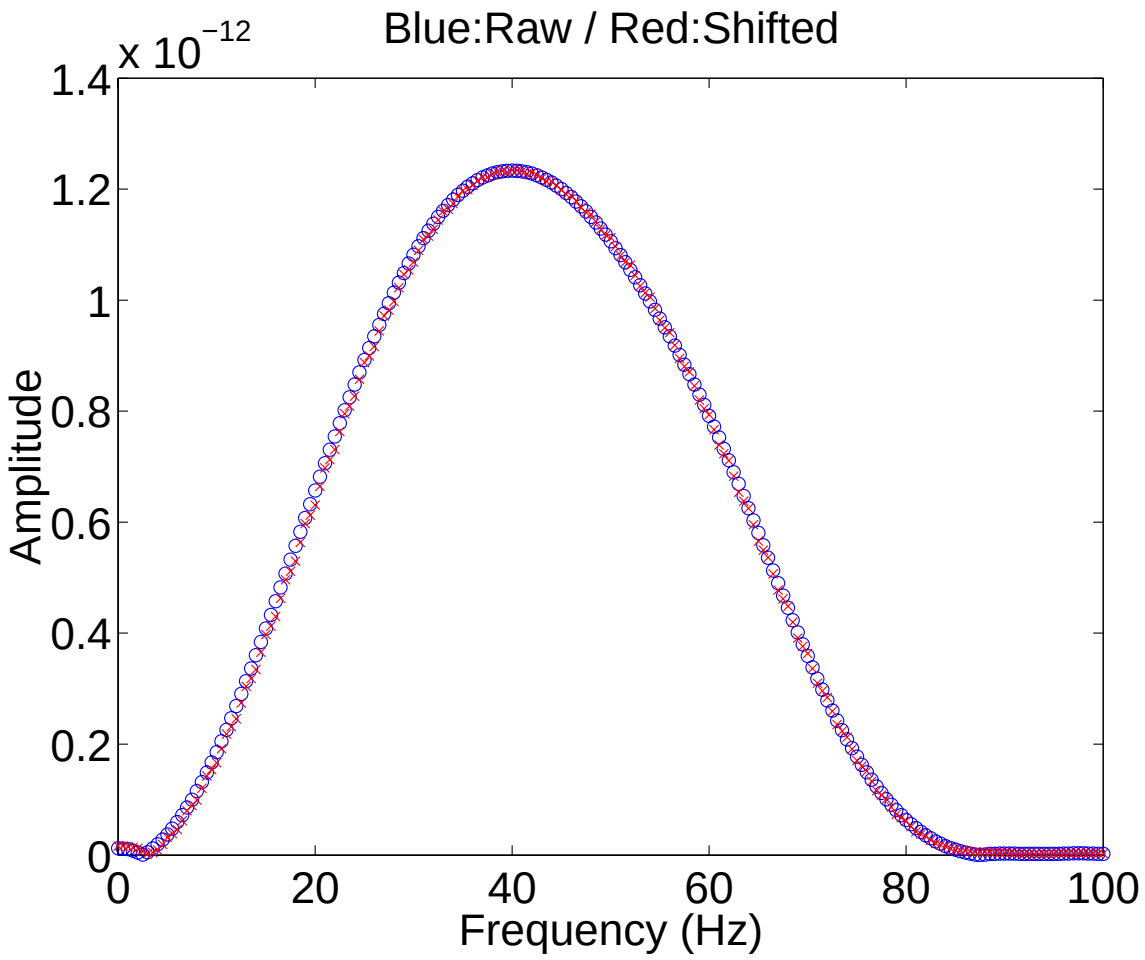

Fig. 2.7. Amplitude spectra from an original trace (blue circle) and from a NMO stretch corrected trace (red cross). The frequency distortion due to NMO stretch has been corrected.

2.3.1 Simple example: Layer over half space

The same full waveform synthetics from this layer over half space model (Figure 2.4) can be used for more complete tests of the method as a function of offset. As explained before, by shifting the Fourier components and by dividing amplitudes using the stretch amount in frequency domain, we can reverse NMO stretch effect. The amount of frequency shift (stretch ratio) can be estimated quite accurately using the equation which is a function of offset, NMO velocity, and zero offset time (Dunkin and Levin, 1973). To test the effectiveness, an extreme case (shallow and far offset trace) is considered. As traces go to far offsets, the widths of wavelets increased due to NMO stretch.

Two 3000 m offset traces from a shallow event (before and after NMO) are shown in Figure 2.8a. In this ideal case, exact values for stretch ratio and amplitude before NMO are known. The numerical estimates that are computed from equation 2.1 and the exact values of stretch ratio that are measured from synthetics are shown at Figure 2.8b. Maximum amplitude values of the 3000 m offset trace before-NMO, after-NMO, and after-stretch corrections are shown in Figures 2.8c-d. After the target oriented NMO stretch correction, the correct amplitudes have been recovered. Percent errors on amplitude after stretch correction (Figure 2.9a) shows less than 5 % over all offset ranges. Figures 2.9b-c show time-frequency representations based on wavelet matching (Liu et al., 2004) of these traces. Amplitude and frequency information matches well while the after-NMO trace shows severe distortions in the values of amplitude and frequency.

2.4 Multi layered model (no thin layer, no tuning)

A multi layered model (Figure 2.10, model parameters from Dunkin and Levin, 1973) has also been used to confirm the effectiveness of our correction and to study the amount of NMO stretch distortions with offset and depth changes (Figure 2.11). The severe distortions of wavelets in the first shallow event are clearly visible, while the amount of stretch decreases with depth. For comparison purposes, only strong signals (1st, 3rd, 4th, and 6th) were corrected for NMO stretch. The time-frequency representations for data from the multi layered model are shown in Figure 2.12 on a mid offset (1800 m) and a far offset (3000 m). Severe distortions in amplitude and frequency on traces from the far offset and the shallow event were observed and

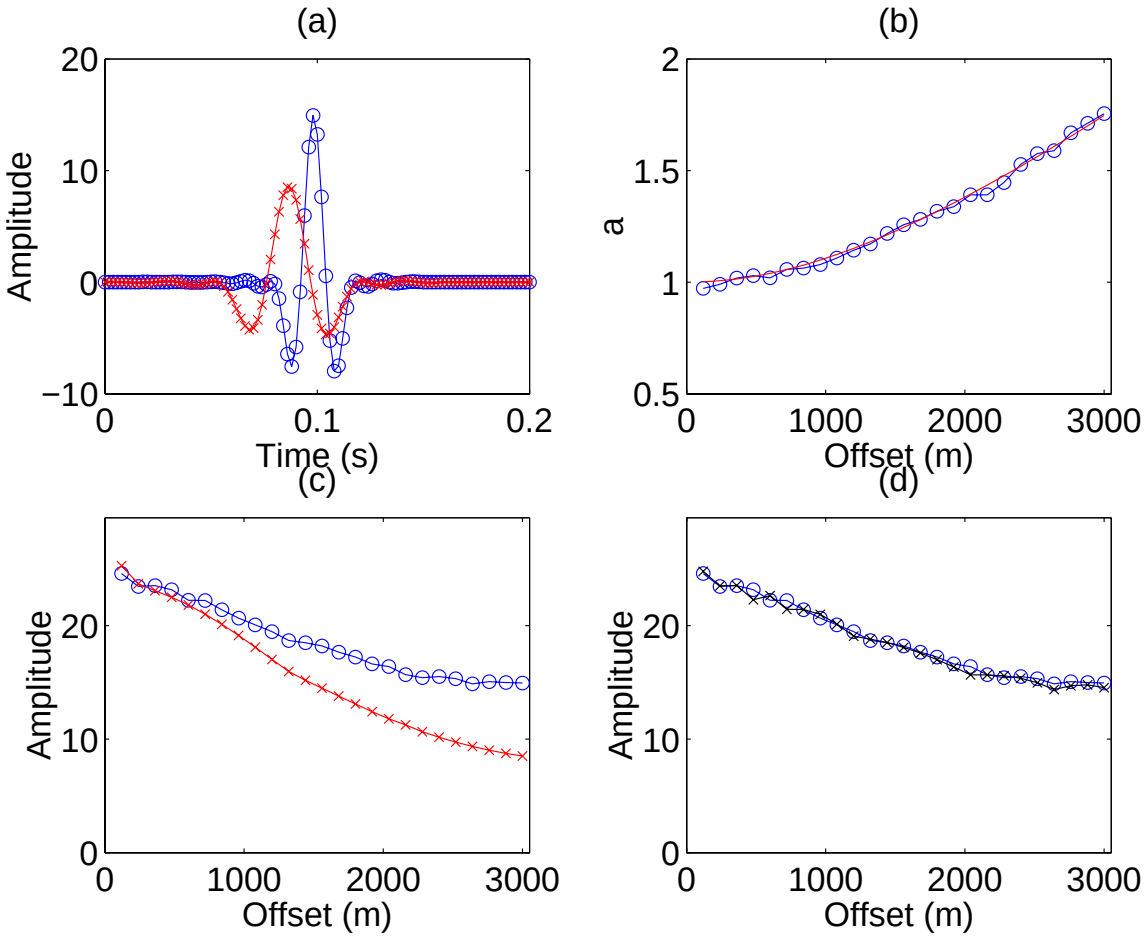

Fig. 2.8. Comparisons among before-NMO, after-NMO, and after-stretch corrections. (a) 3000 m offset traces (blue: before-NMO, red: after-NMO), (b) Stretch ratio (blue: computed from input data, red: estimation using the Dunkin and Levin (1973)'s equation). (c) and (d): Absolute maximum amplitude of wavelets of before-NMO (blue), after-NMO (red), and after-stretch corrections (black).

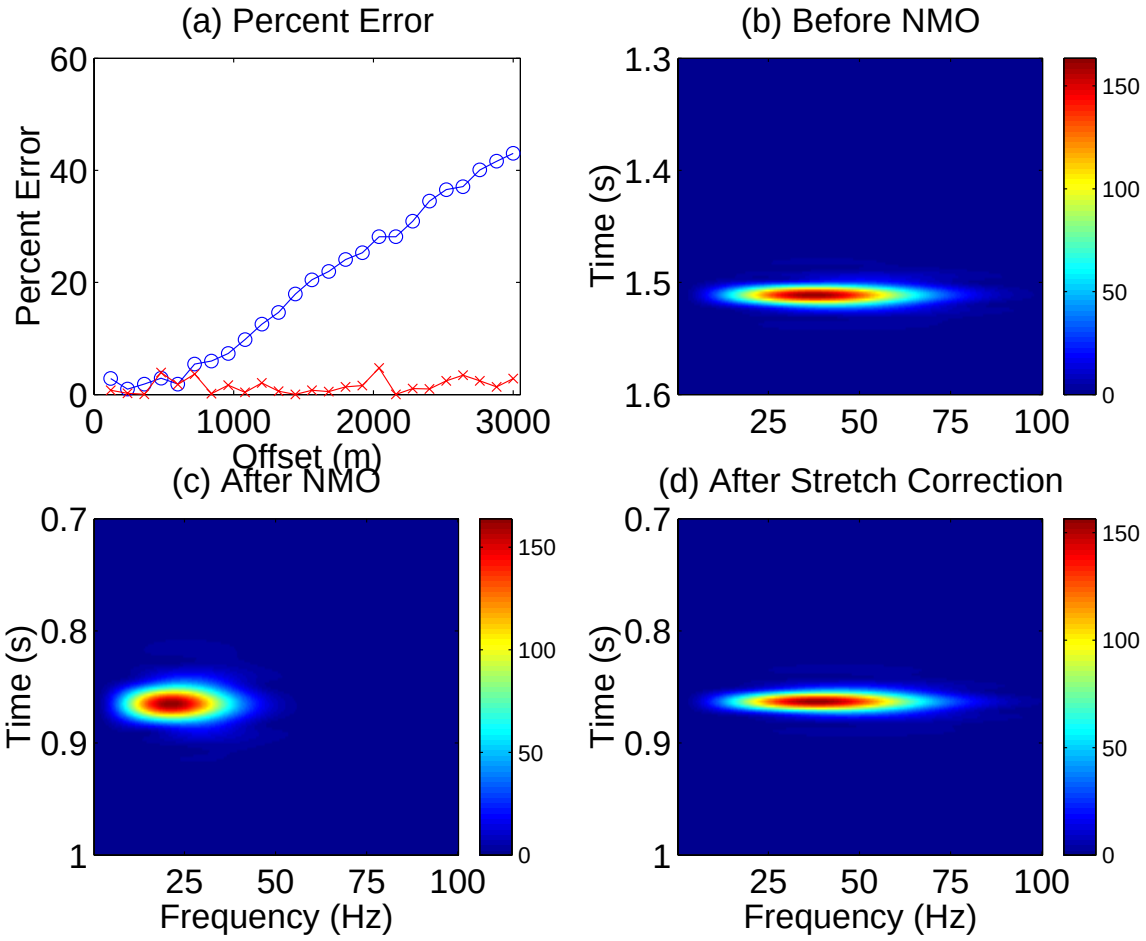

Fig. 2.9. (a) Percent errors in amplitudes before and after stretch correction with respect to amplitudes before NMO. It show less than 5% error. Time-frequency representations based on wavelet matching (3000 m offset trace). (b) Before-NMO (answer), (c) after-NMO, and (d) after-stretch corrections. Notice the similarity of frequency contents after the stretch correction.

corrected.

2.5 Two thin layers model

Using well log information from Ursa field, deep water GOM (Figure 2.13), we designed a simple but realistic test model to compute synthetic seismograms to see what to expect in later field data applications. Specifically, we are interested in frequency-dependent AVO effects that might be caused by changes in pore fluid contents, such as attenuation. Therefore we introduce arbitrary values of attenuation into a simplified velocity model based on the field data to see what effects might be detected in AVO. The two thin layer model is shown in Figure 2.14. Based on the laboratory experiment result that fizz reservoirs would exhibit strong Q, we included additional model parameters of Q of infinity or 5 in the upper fizz reservoir.

After windowing reservoir area to minimize computational cost, NMO stretch correction, spectral decomposition, and attribute inversion have been applied. After applying this workflow, Figure 2.15 shows the crossplots of NI and gradient from upper fizz and lower oil reservoirs while correcting NMO stretch for more accurate spectral analysis. Before (Figure 2.15a and b) and after stretch correction (Figure 2.15c and d), spectral variations among 20-50 Hz have been corrected. For example, points from high frequency (50 Hz) changed most while ones from other frequency slices moved to the correct locations. The major difference between two models (no Q and Q of 5) can be identified as the overall decrease of the trend (line-fit) with more decrease in gradient values (Figure 2.15c and d). Also, we can observe more decrease in data points from high frequency which agrees with our expectation from Q theory. We observed the similar result in the lower oil reservoir case from the NMO stretch correction while decreasing only NI values in different Q models (Figure 2.16). This can be explained by loss of energy from passing through the upper layer with strong Q. From this series of test, we learned that effects of Q in a layer and its consequence to other layers below it.

2.6 Conclusions

The frequency and amplitude distortion due to NMO stretch can be corrected using Dunkin and Levin (1973)'s derivation. Using a simple and a multi layer model,

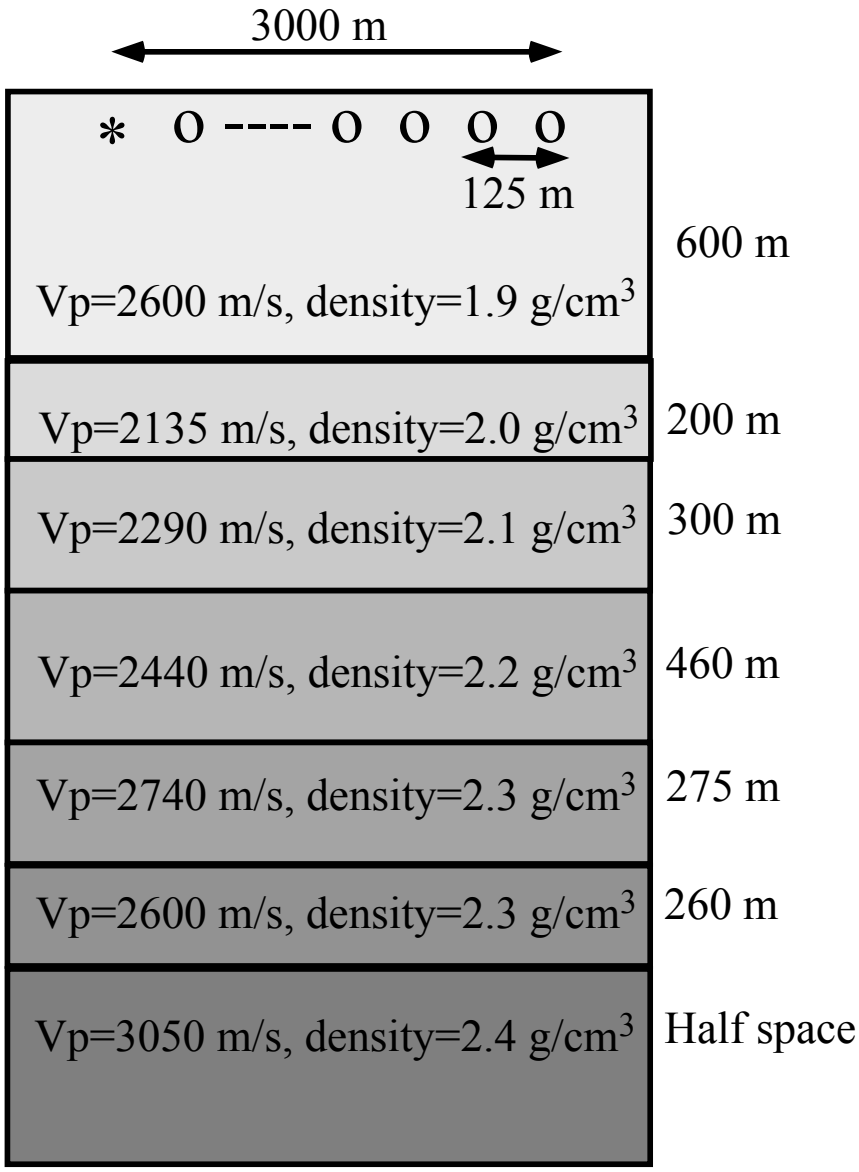

Fig. 2.10. Model parameters and acquisition geometry for a simple model. * represents source location and o receiver locations.

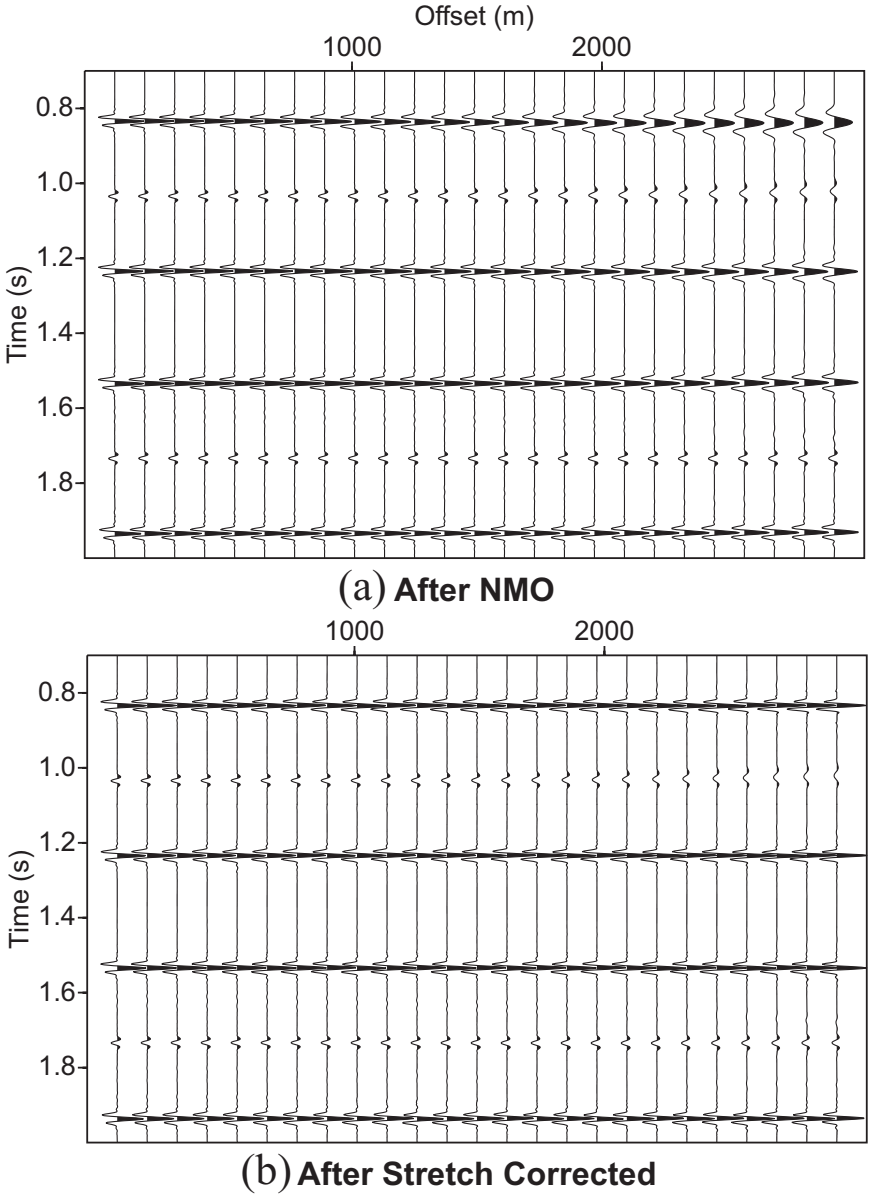

Fig. 2.11. Vertical components of full waveform synthetic from the Dunkin and Levin (1973) model. After the target oriented stretch correction, the time resolution has increased. Note that only 1st, 3rd, 4th, and 6th events were stretch-corrected and AGC has applied to see waveforms of deeper events better.

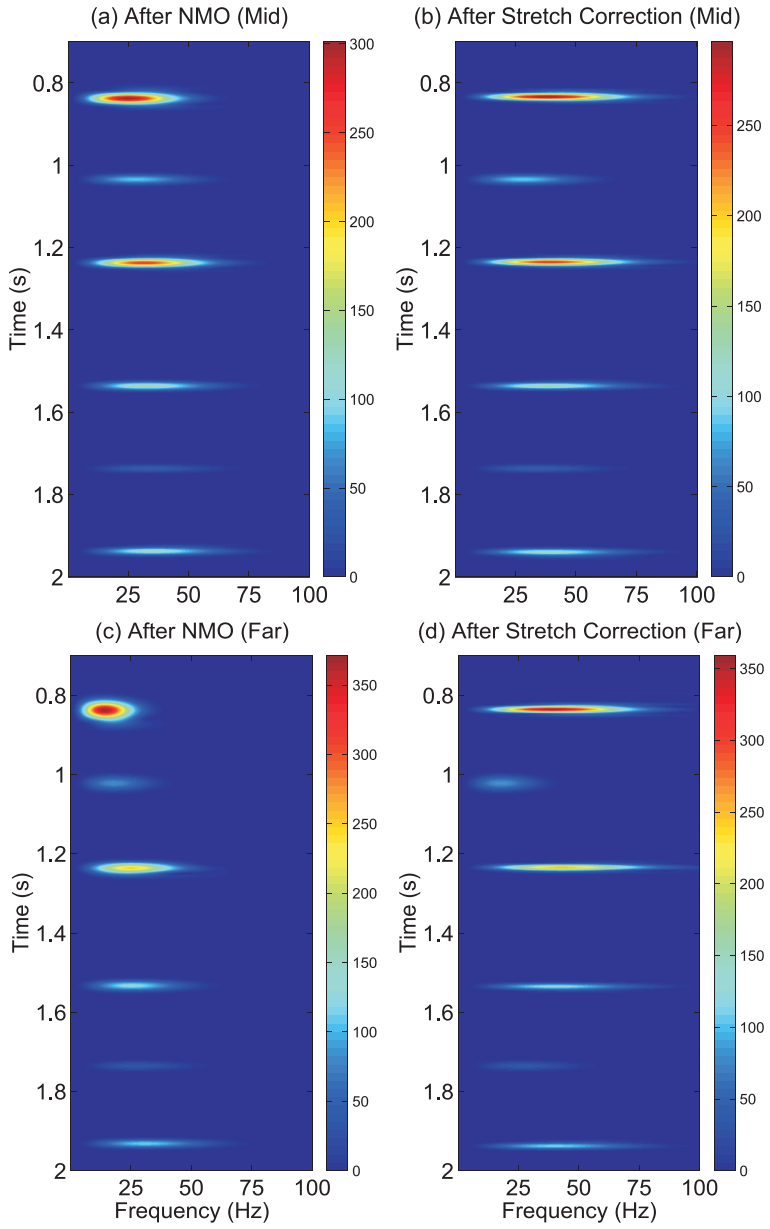

Fig. 2.12. Time-frequency representation of mid (1800 m) and far offset (2900m) traces from Dunkin and Levin (1973) model. For comparison, only 1st, 3rd, 4th, and 6th events were stretch-corrected. As expected, shallow and far-offset events show large amount of corrections. No AGC has applied to the input synthetic in these TF representations.

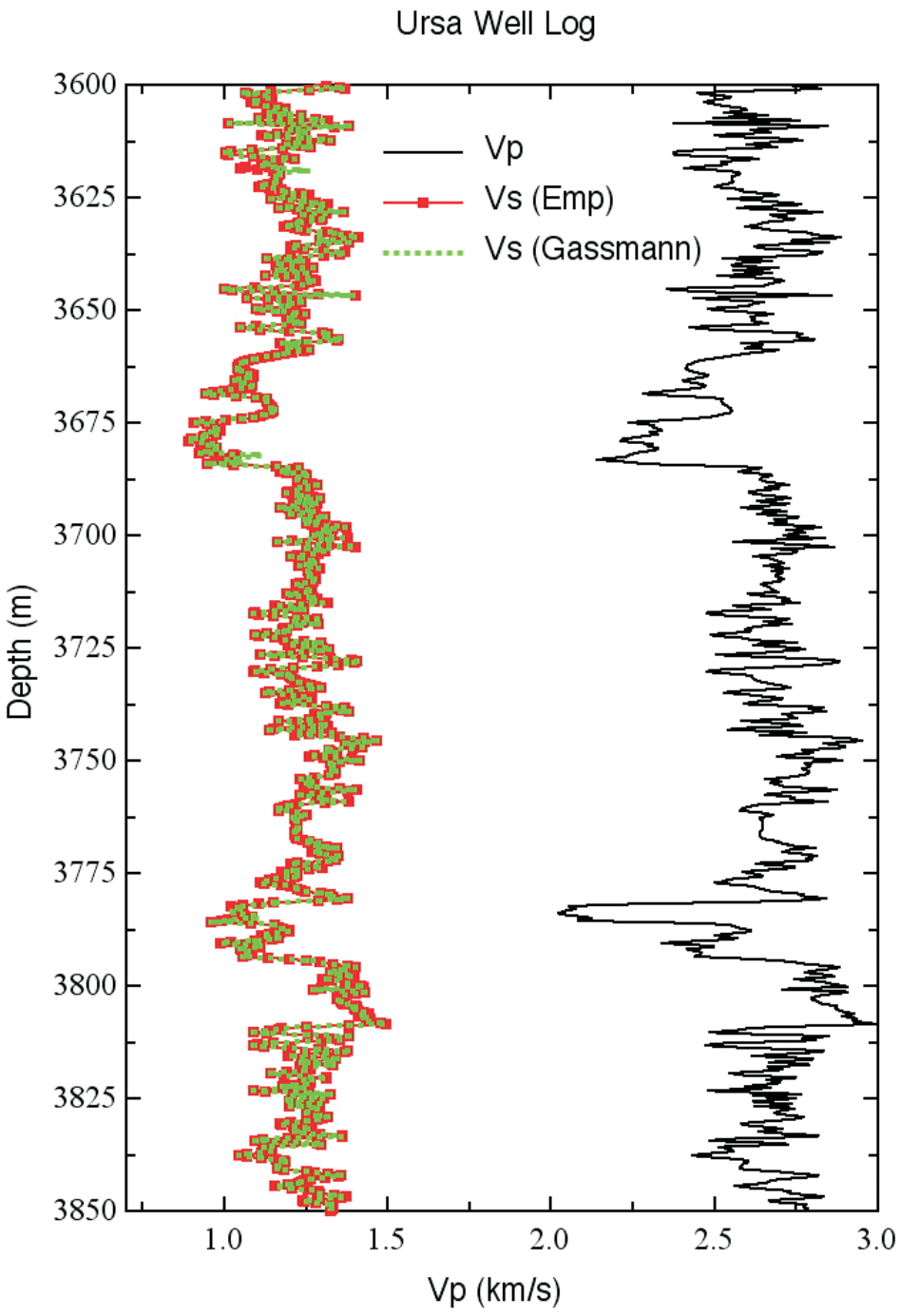

Fig. 2.13. P-wave velocity from sonic log. Also, derived S-wave velocities using empirical relations and Gassmann equations are shown.

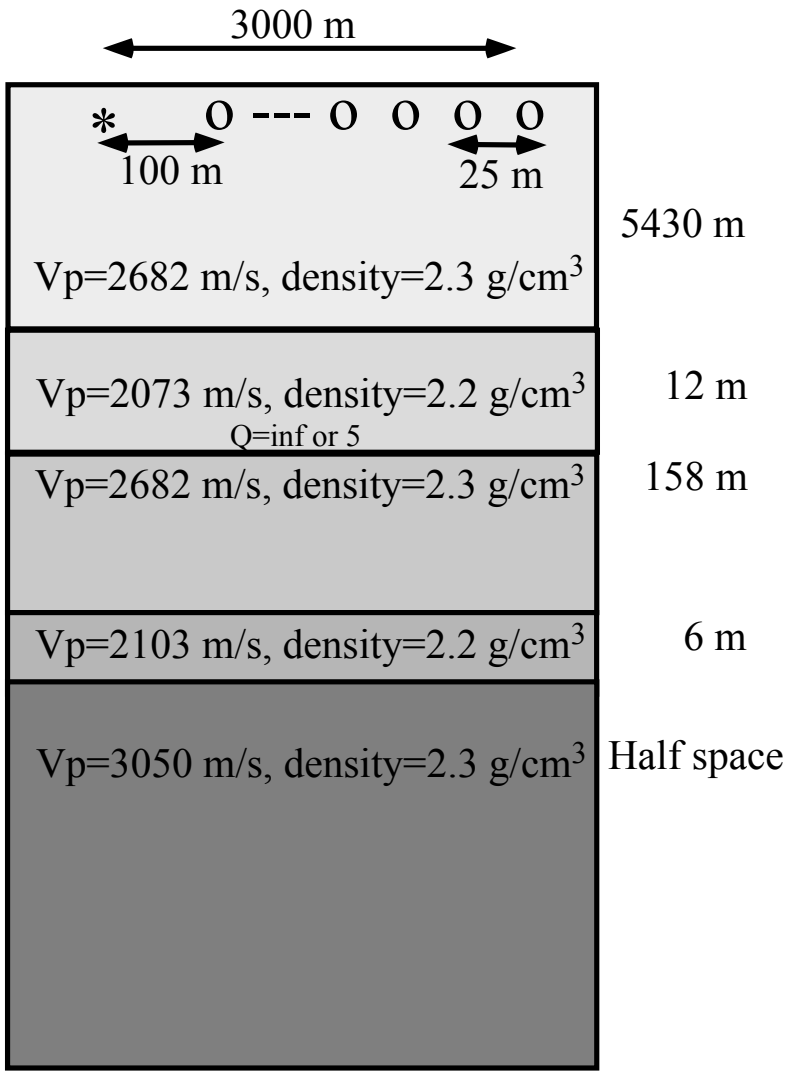

Fig. 2.14. A simple model for the synthetic computation based on well log information. * represents source location and o receiver locations.

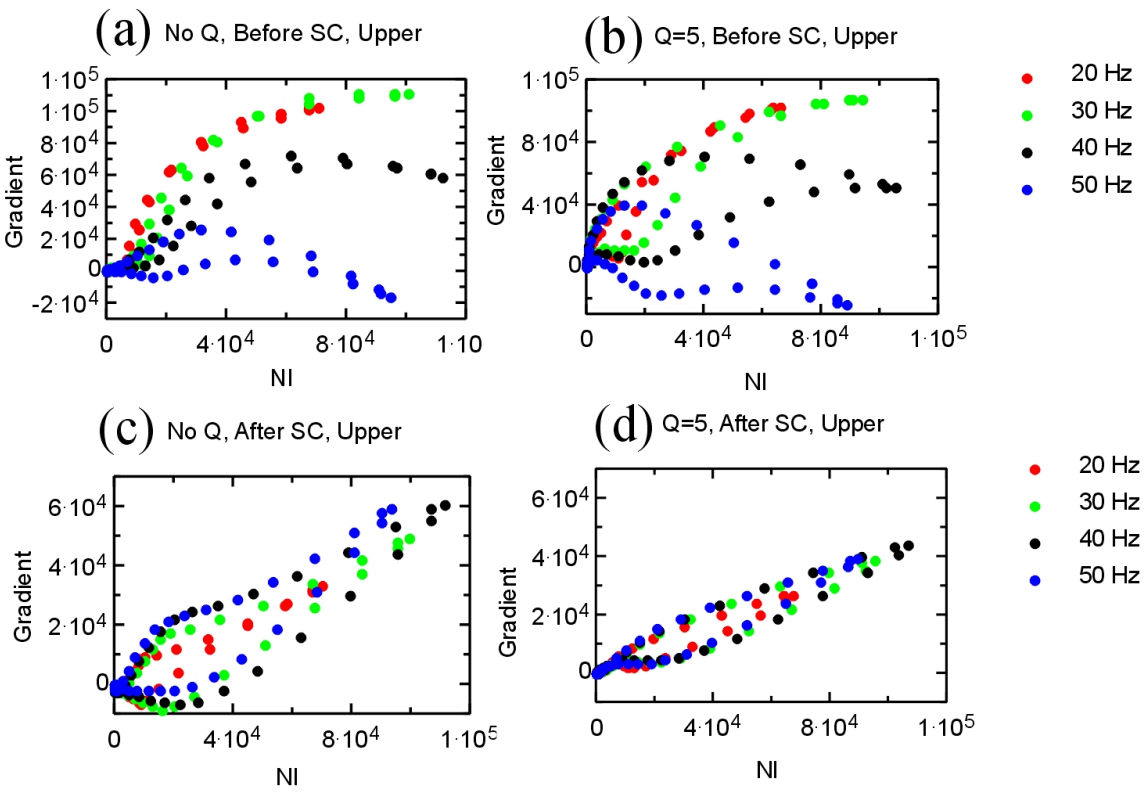

Fig. 2.15. Crossplots of NI and gradient from upper fizz layer model.

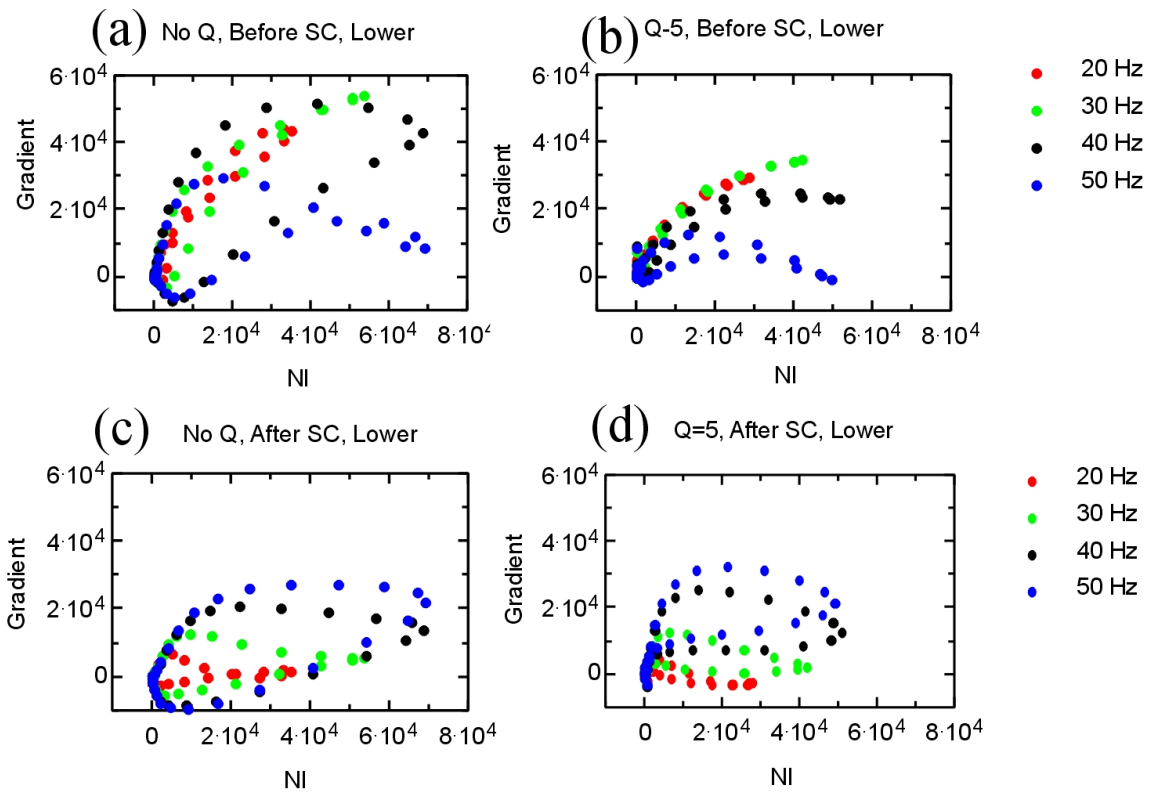

Fig. 2.16. Crossplots of NI and gradient from lower oil layer model.

we verified that our target oriented stretch correction scheme can recover distorted frequency and amplitude information. For more accurate AVO inversion process, we added an wavelet alignment process that is based on crosscorrelation. An additional process that can handle noisy data needs to be developed and will be addressed in the later chapter.

CHAPTER III

APPLICATION OF FREQUENCY DEPENDENT AVO WORKFLOW TO TEAL SOUTH, SHALLOW WATER GOM

3.1 Introduction and summary

The tests on synthetic seismograms presented in the previous chapter show that we have an effective procedure for correcting NMO stretch errors, applying time-frequency spectral analysis, and assessing frequency dependent AVO. Applications to field data will help reveal the effectiveness of this workflow when errors and noise are present in the data. One good candidate for these tests is field data from the Teal South test site, which includes 4-D measurements using ocean bottom seismometers (OBS).

The NMO stretch correction scheme will be important due to the shallow water depth and reservoir locations. Also, significant amount of time processing has been done by a contractor already (details in the preprocessing section), which enables us to test our claim that this workflow can be used on top of an existing seismic processing flow for further analyses.

A series of elements for frequency dependent AVO workflow that is used for synthetics in previous chapter is applied to two target events, known as 4500 ft and little neighbor (Pennington et al., 2001), for improved reservoir characterization. By choosing known anomalous events, we can compare our result with existing AVO studies available on those targets, which is known to show Class III AVO anomaly. After the stretch correction, we could observe systematic increases mainly in magnitudes of the AVO gradient attribute. As expected from NMO stretch characteristics, the low frequency region has been less affected while mid and high frequency regions were affected considerably. In seismic attributes analysis, the attribute crossplots from spectral decomposed prestack data confirmed the improved accuracy and effectiveness of our workflow in mid and high frequency regions.

3.2 Data description and preprocessing

This 4D/4C OBS data set is acquired over 9 km^2 in Eugene Island Block 354 (Figure 3.1), using a shot grid of 25 m by 25 m over two periods of time (year 1997 and 1999). Previously, another legacy data from towed streamer is acquired in 1995, but we used the most recent one from year 1999 that showed the best S/N ratio. In their most recent two OBS acquisitions, the goal was to build a low cost 4D/4C permanent reservoir monitoring system. Two phases of data (Phase 1 in year 1997, Phase 2 in year 1999) were available for our analysis. Figure 3.2 shows shot, mid-point, and receiver geometries in the two time lapse surveys. Located below 85 m of water, the reservoirs were positioned within a series of mini basins at the depth from 1300 to 2400 m. The average reservoir thickness is about 70 m and the target of this study (4500 ft sand) is bounded by normal faults (Andre and Rinehart, 1997).

In Figure 3.2, note that the Phase 1 survey only included 24 receivers on the left side. A series of source lines with 25 m shot-spacing and 25m line-spacing enabled significant fold coverage over several reservoir areas, especially for Phase 2. The CMP bin size was 12.5 by 10 m with maximum folds of 24 for Phase 1 and 32 for Phase 2. Because there were 40 more shot lines in Phase 2, the range of CMP numbers is larger for this second experiment. Specifically, the values of CMP in the E-W direction range from 1040 to 1254 for Phase 2, but only from 1040 to 1199 for the Phase 1 survey. Overall, data quality was better in Phase 2, but three near offset traces were severely contaminated by low frequency noise consistently in this Phase 2. This will make the application of Lazaratos and Finn (2004)'s method difficult because their method is based on the wavelet deconvolution using wavelets from near offset. Some other suboptimal data conditions include severely stretch muted far offset traces (difficult for our target oriented stretch correction), less fold and poorer S/N ratio in Phase 1 data (difficulty for direct comparison with phase II), and irregular offsets among CMP gathers (difficulty for data handling).

Commercial contractors applied a conventional processing flow to the field data to prepare the CMP gathers, and a summary of the major steps is shown in Figure 3.3. This defines the initial status of the data that we have available. After a careful examination of the available documentation describing this processing, we identified several processing steps where seismic amplitudes have been arbitrarily altered for conventional stacking and imaging. A time variant scaling (3 - 6 dB/sec)

Fig. 3.1. Location of Teal South field for 4D OBS data (Source: Google available at http://maps.google.com/).

that increased amplitude at late times was applied to amplify deeper reflections. An offset-dependent correction was also applied to strengthen far-offset amplitudes. These types of gains were routinely applied for the correction of average attenuation effects that are related to average rock properties and wave propagation (geometrical spreading). These gains will compensate for the average overburden attenuation effects so that we can focus to the attenuation effects at the reservoir level.

3.3 Conventional and frequency dependent AVO analysis after stretch correction

Following the initial waveform analysis, three overlapping ranges of band pass filters (frequency parameters for each trapezoidal filter: 4,8,28,25 Hz for Low, 18,25,45,52 Hz for Mid, 35,40,60,90 Hz for High) were applied and the intercept and gradient attributes were interpreted, which will give us some indications as to how to use the spectral information. The full band data showed the peak frequency at 35 Hz and two other center frequency for Low and High region for bandpass filter were carefully chosen at 18 Hz and 50 Hz respectively to represent low and high frequency data content. Figure 3.4 shows the cross-plot of normal incidence and gradient. The major reason why we are looking at different frequency range here is that different

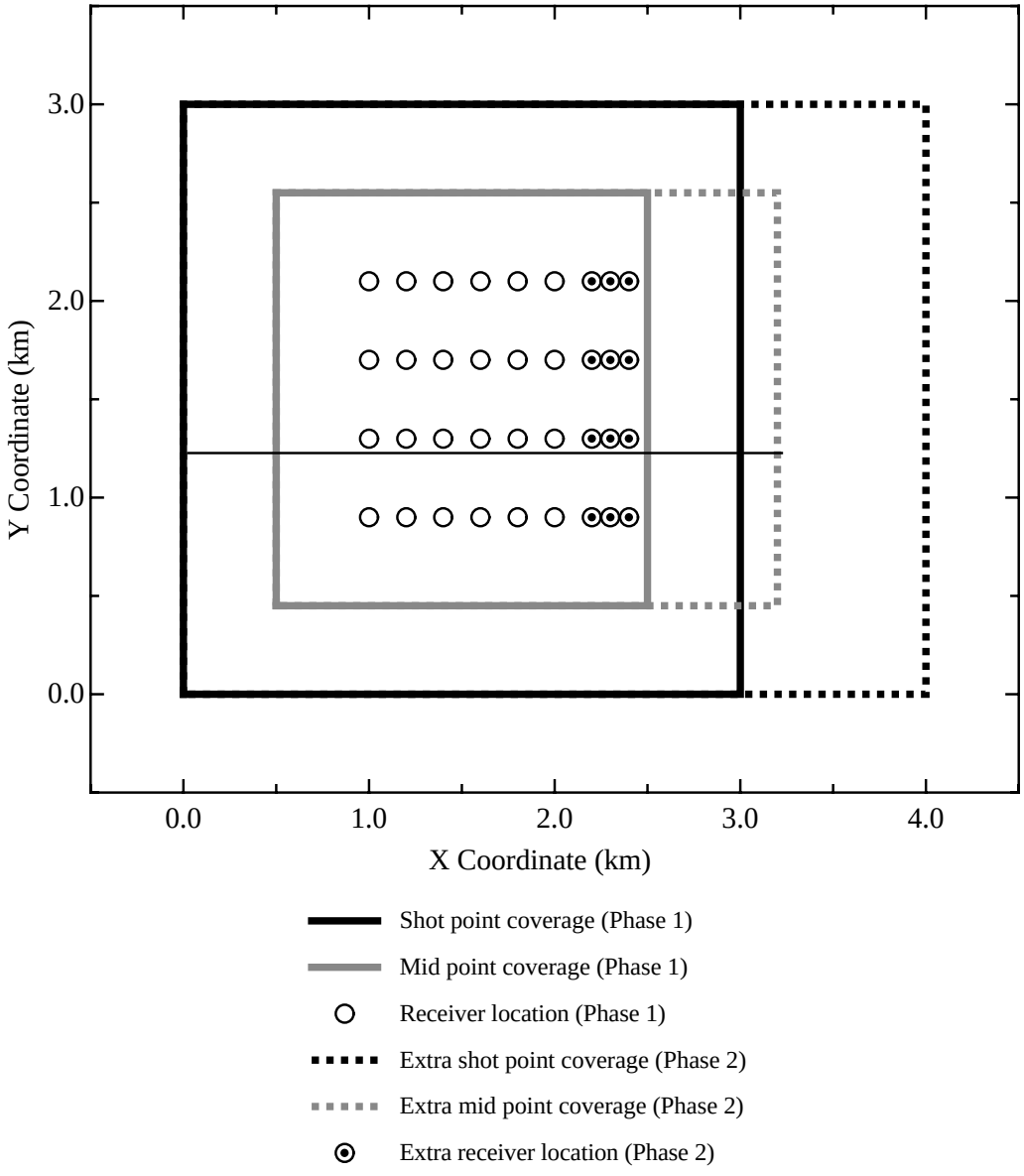

Fig. 3.2. Acquisition geometry of Teal South 4D OBS data. A horizontal line at about 1.25 km of Y axis represents the inline location of the analyzed data.

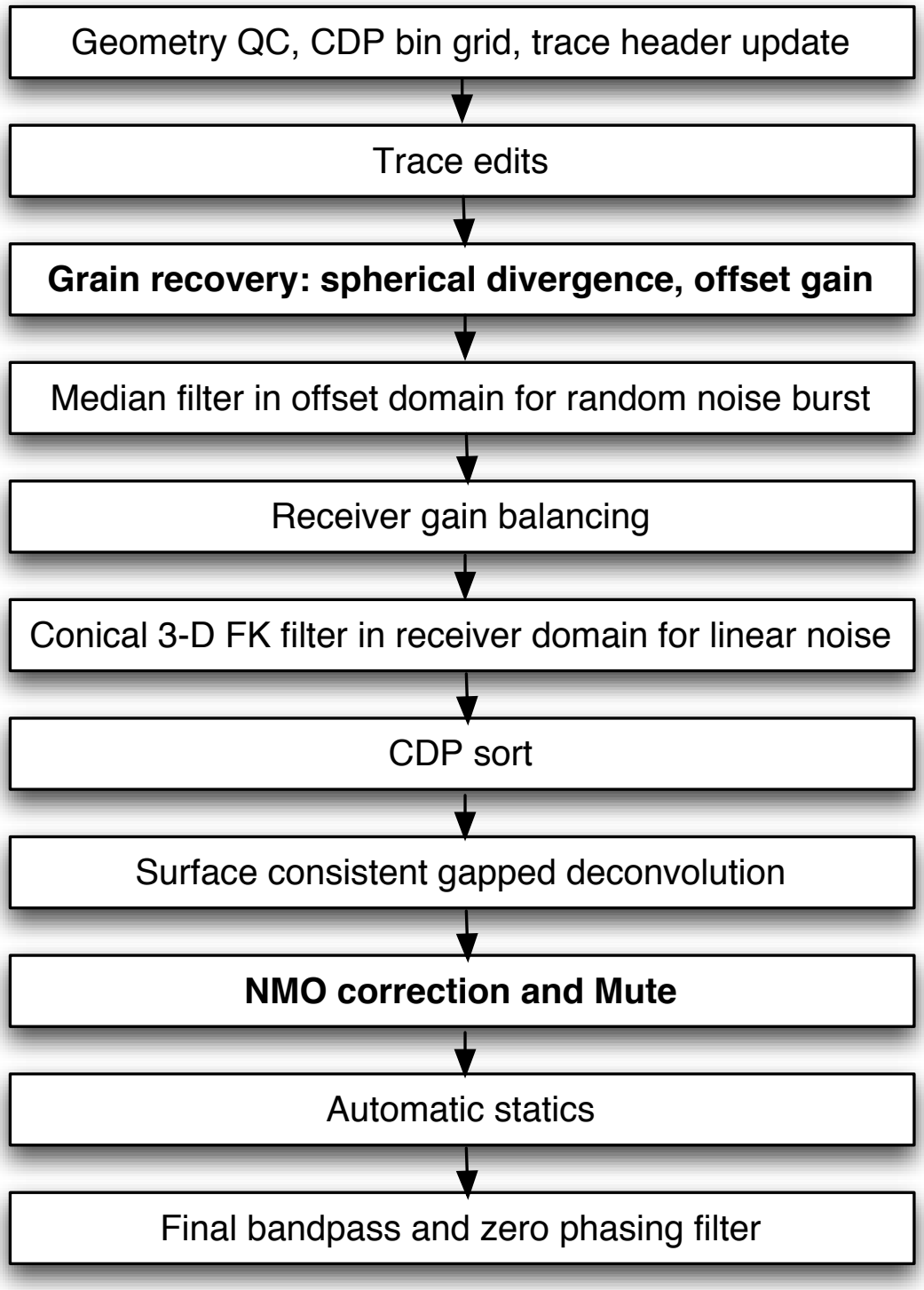

Fig. 3.3. Time processing workflow that has been applied to Teal South.

constructive and destructive interference will occur among different frequency ranges resulting in some differences at AVO cross-plots. After dividing the CMP gather into three regions, we defined a background anomaly and excluded those backgrounds in the cross-plots to pick anomalous regions. At the low frequency data, a trend of being elongated into first and third quadrants was observed. At the mid frequency data where the dominant frequency was the same as the full bandwidth data, the anomaly pick was the most identical to that from the full bandwidth data. At high frequency data, we can notice that the anomaly in the cross-plots is not easily distinguishable anymore. This effect was coming from NMO stretching artifacts where high frequency contents were affected more than the low frequency signal did.

Within the two known hydrocarbon zones (Pennington et al., 2001) from the time lapse data, we picked 20 CMP gathers near the 4500 ft sand and 10 CMP gathers near the little neighbor for an AVO attribute analysis. After careful choices of the stretch ratio threshold, the application window length, and the taper size, we applied the target oriented stretch correction only to the events of our interest (Figure 3.5).

After our target oriented stretch correction, narrower wavelets are clearly visible at far offsets. Also, the additional scheme based on crosscorrelation, which was explained in previous chapter, significantly improved the alignment of events (Figure 3.5b). We performed a further test using crossplots of AVO attributes of normal incidences and gradients to see how significant amount of changes were done after our stretch correction. First, the crossplots from two events (4500 ft sand and little neighbor) were compared. Figure 3.6 shows normal incident (NI) and gradient cross plots of these two reservoirs before (Figures 3.6(a)-(d)) and after (Figures 3.6(e)-(f)) stretch corrections. In this conventional AVO analysis, it is clearly visible that many points in the upper left and lower right quadrants systematically moved to upper right and lower left quadrants in the 4500 ft sand case (Figure 3.6a and e). These random points occur due to the NMO stretch or the misalignment of events. On the other hand, we do not see a very large amount of change in the little neighbor case (Figure 3.6c and g).

Further analysis using time-frequency representation has done and AVO attributes were computed on three frequency slices (20, 35, and 50 Hz). After constructing frequency cubes by spectral decomposition (Figure 3.7), we inverted the amplitude for normal incident and gradient attributes. I would like to reemphaze that we are analyzing a single frequency slice from prestack CMP gathers rather than

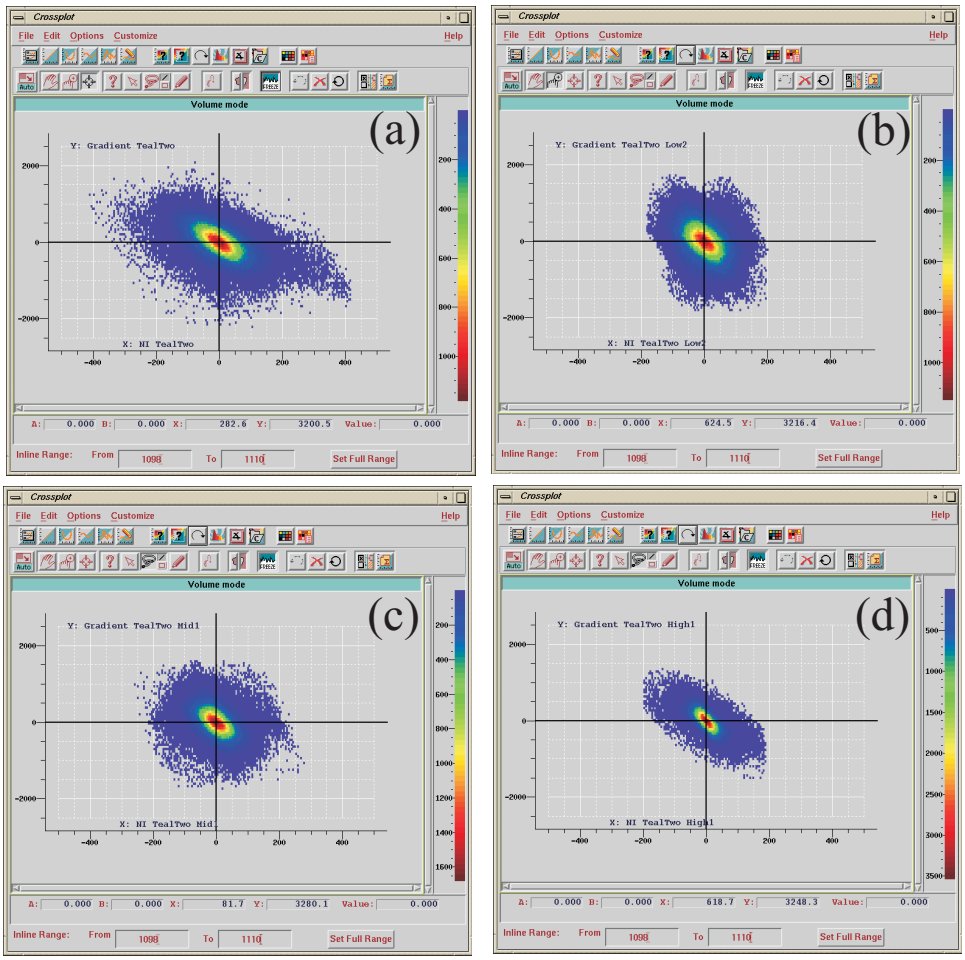

Fig. 3.4. Cross-plots from (a) Full bandwidth data, (b) Low frequency data (filter parameter: 4,8,28,25), (c) Mid frequency data (18,25,45,52),(d) Low frequency data (filter parameter: 35,40,60,90). Notice the different shape on the cross-plots from low frequency data and hard-to-pick anomaly in high frequency data.

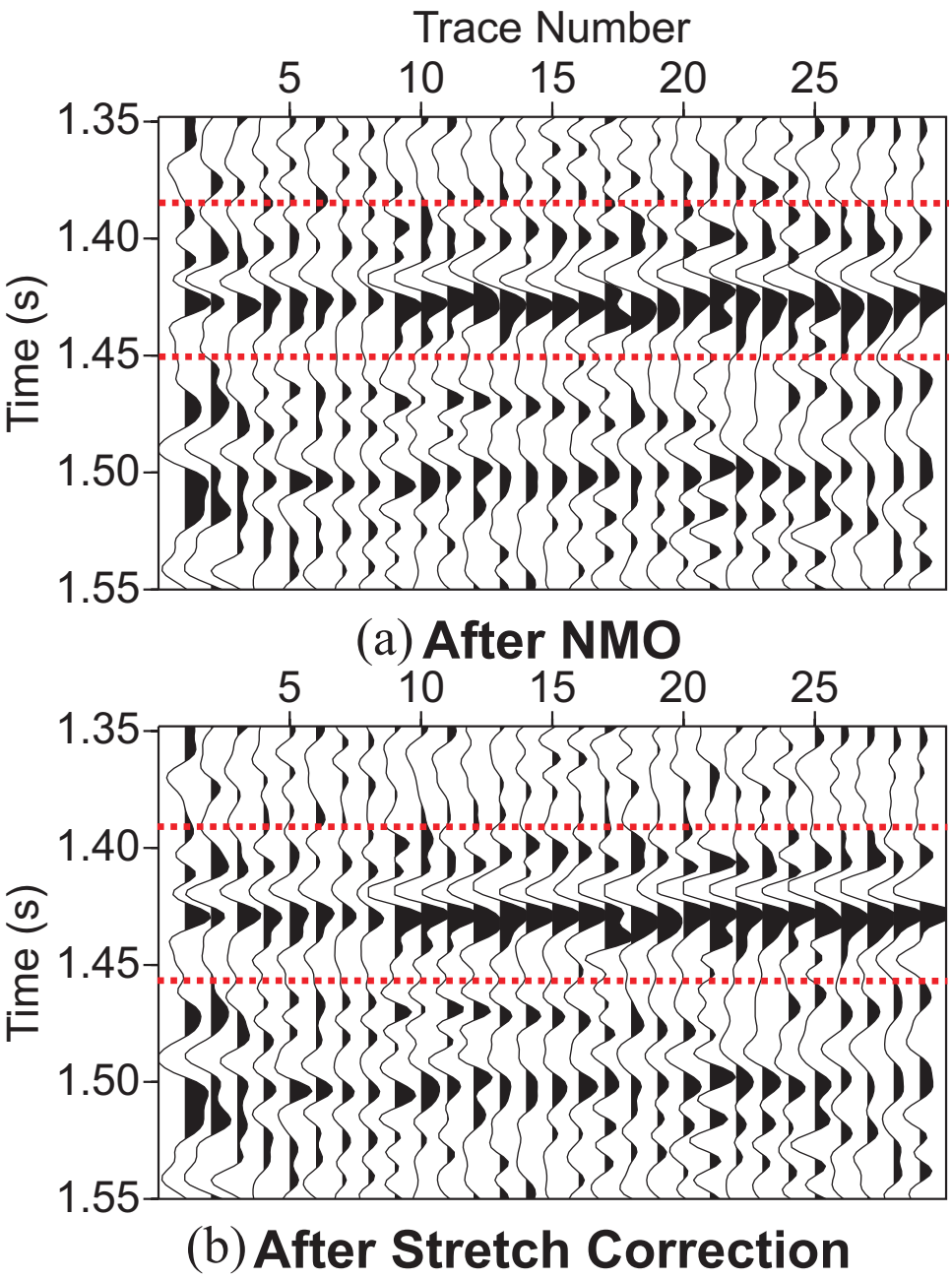

Fig. 3.5. Teal South CMP gathers (10981144) (a) before and (b) after stretch correction. The resolution of far offset reflections and the alignment of reflections have been improved: clearly visible at far offsets. Using stretch ratio threshold of 1.01, traces after the 4th are corrected for NMO stretch.

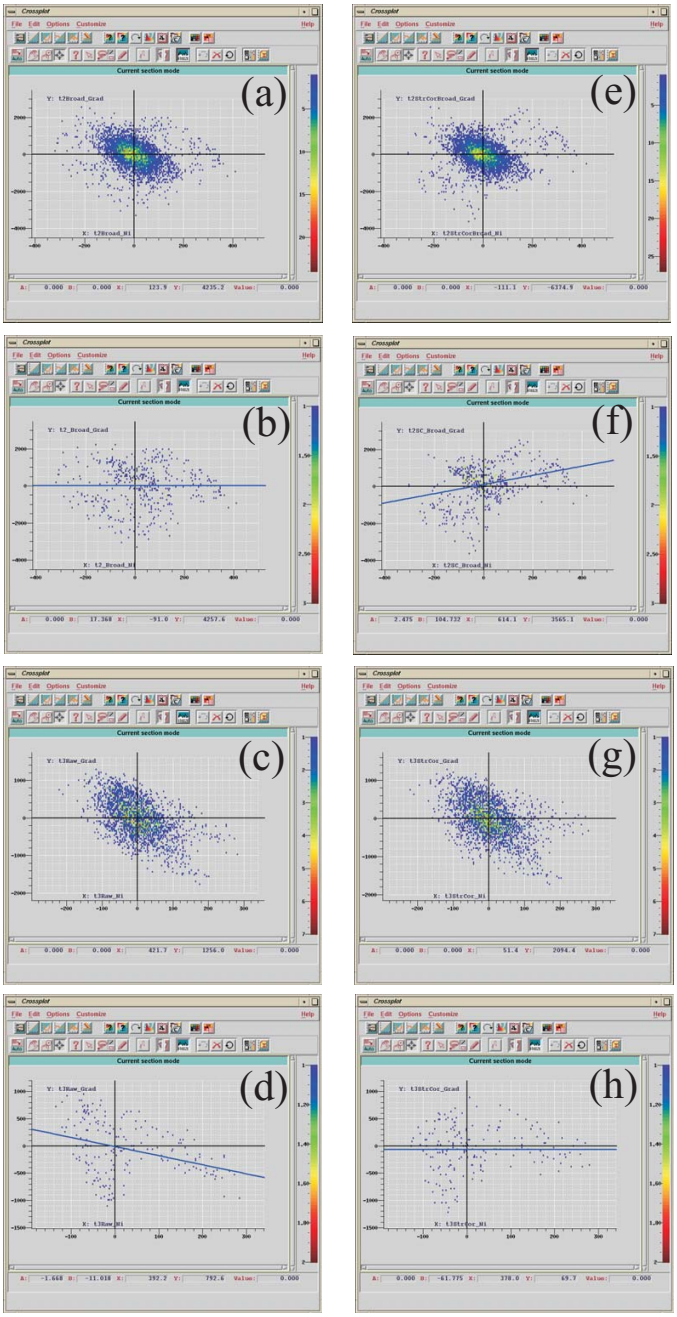

Fig. 3.6. Cross plots of normal incidence (x-axis) and gradient(y-axis) AVO attribute. (a)-(d):Before stretch correction. (e)-(f):After stretch correction. (a) and (e): 4500 ft sand all CMP gathers, (b) and (f): 4500 ft sand reservoir only, (c) and (g): little neighbor all CMP gathers, (d) and (h): little neighbor reservoir only.

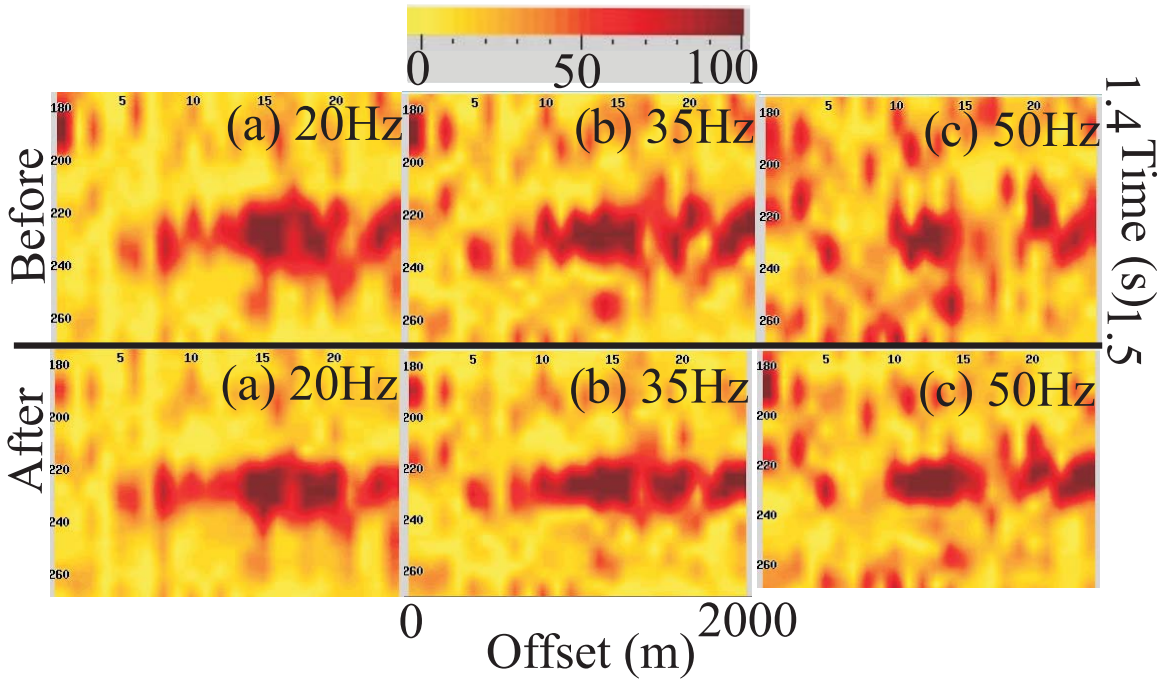

Fig. 3.7. Spectral decomposed CMP gathers at 20, 35, 50 Hz. (a)-(c): Before stretch correction. (d)-(f): After stretch correction. Notice better alignments and amplitude corrections in mid-high frequency slices after stretch correction.

one from a full band data in previous examples. As expected, slight decrease of amplitude was observed at the 20 Hz slice and significant amounts of amplitude increases were clear at 35 Hz and 50 Hz slices (Figure 3.7). The crossplots of spectral decomposition are different from conventional ones because all amplitudes values are positive (Figure 3.8). Here, background trends are located over the upper left and lower left quadrants. We observe systematic increases of gradient values especially in mid and high frequency slices. Major difference comes from negative normal incidence values due to some strong gradient values, which originates from strong anomalies. These points were plotted in the upper left quadrant rather than the upper right quadrant, which makes more clear separation. By comparing Figure 3.8 (a)-(c) (before stretch correction), this result could be misinterpreted as showing strong frequency dependent AVO effects: Anomalous region of upper left quadrant is strong at low frequency data (a). On the other hand, after stretch correction in Figure 3.8 (d)-(g), we see balanced AVO plots, where all frequency data show AVO anomaly at upper left quadrant. We can conclude in the future that, after the stretch correction, if we see the plots like (a)-(c), the reservoir yield strong low frequency effects. We might be able to further

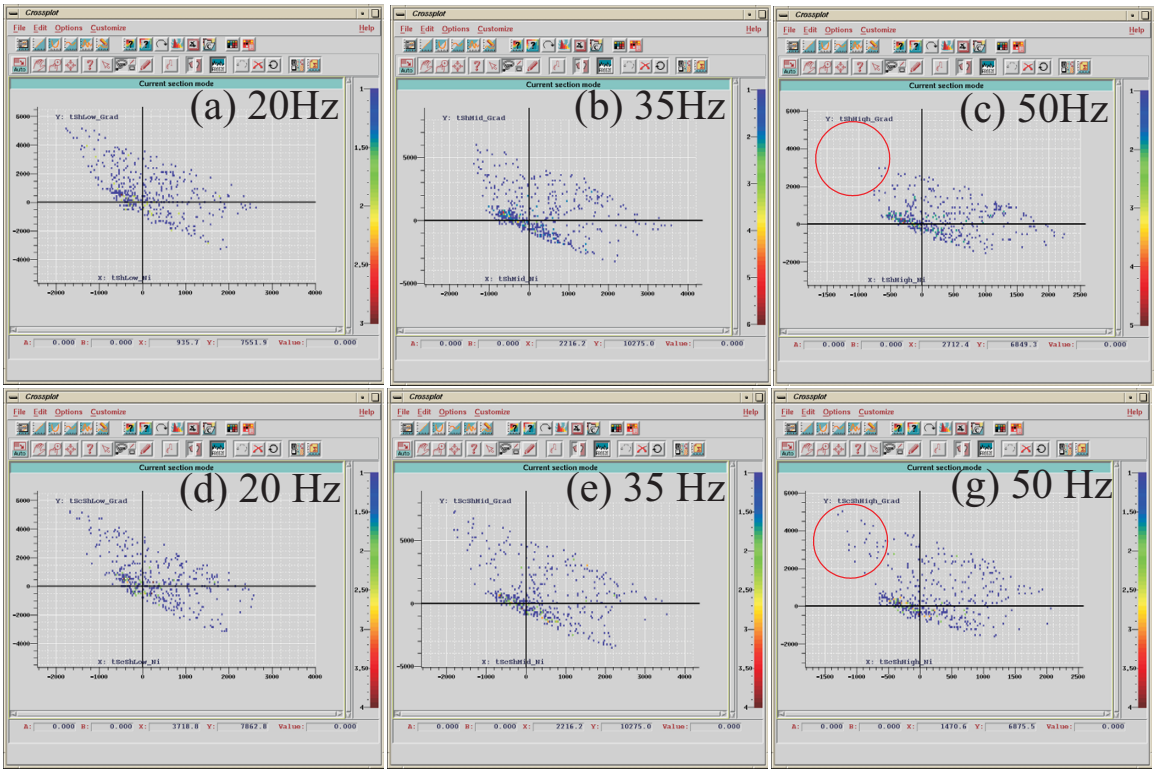

Fig. 3.8. Crossplots of normal incident (x-axis) and gradient (y-axis) from reservoir events only after the spectral decomposition. (a)-(c): before stretch correction, (d)-(f): after stretch correction. Notice significant increase in gradient attributes in 35 and 50 Hz.

quantify the observation through synthetics and detailed AVO crossplot study.

3.4 Conclusions

A simple but robust stretch correction algorithm has been tested over a field data set from Teal South, GOM. Our target oriented approach is computationally very effective because it only applies to the events of our interest while not losing much information. It corrects amplitude and frequency information for far offset effectively: no need to apply strong mute throwing away probably important far offset information. Most importantly, it can be used on top of existing time processing workflow and can be used as an risk assessment tool at the end. We showed that frequency dependent AVO analysis result will be only valid after the stretch correction, recovering lost mid and high frequency information. Unlike conventional AVO analysis,

anomalous region is plotted on the upper left quadrant of NI and Gradient attributes. It was shown that without stretch correction, the results could be misinterpreted as showing frequency dependent effects.

CHAPTER IV

ROBUST FREQUENCY DEPENDENT AVO WORKFLOW: URSA, DEEPWATER GOM

4.1 Introduction and summary

The success of our frequency dependent AVO analysis algorithm depends on the quality of preprocessed data. In other words, we need to preserve amplitude and frequency information for an accurate frequency dependent AVO analysis. There are many preprocessing considerations such as gain, deconvolution, multiples, and migration methods. For multiple problems alone, it is widely recognized that one specific method cannot solve all multiple problems, and a series of multiple suppression methods should be used to better attenuate free-surface multiples. Currently, the major methods in multiple attenuation can be summarized into the following two groups: (1) wave theory-based (Verschuur et al., 1992; Weglein et al., 1997), (2) move-out discrimination-based. Wave theory based methods of which use data itself as a multiple prediction operator can be thought as a prestack inversion of 2D-wavefield (Dragoset and Jericevic, 1998). Even though their mathematical starting points and view points are different, their final equations to remove surface related multiples are basically the same.

On the other hand, the move-out discrimination-based methods simply use the move-out differences between primaries and multiples. In some cases, primaries and multiples can be easily separated after the Radon transformation of the data into the tau-p (time vs. moveout) domain (Foster and Mosher, 1992). A very comprehensive test (head-to-head comparisons among 22 demultiple methods) using a deep water, sub-salt synthetic data set showed that wave theory-based techniques yielded far superior results than any other methods. Even though the moveout discrimination-based methods literally did nothing in this sub-salt case (Bishop et al., 2001), they are still easy to use and effective enough in many simpler geological settings. In our data set, reservoirs are located at the flanks of salts and Radon based demultiple removed most of multiple energy that interfered with primaries from those reservoirs.

The Teal South data set examined in the preceding chapter had been pre-

Fig. 4.1. Location of Ursa streamer 2D data (Source: Google available at http://maps.google.com/).

processed before we received it, including routine gains and filters, which meant we could not study the influence of these processing elements on our frequency dependent workflow (Figure 3.3). Another set of field data, the Ursa data set, on the other hand, is a raw one which has no processing has applied, and we can therefore process it through all the way to final images and AVO while preserving amplitude and frequency information. Low signal-to-noise ratios can significantly reduce the effectiveness of AVO analysis, so we also implemented a new substack scheme that stacks adjacent traces to increase S/N ratio in this data. Synthetic tests verified the effectiveness of this additional step. After modeling multiples using radon method, we subtracted it from the data set followed by prestack time equivalent migration method for imaging. Applications to this deep water data set showed significant improvement in high frequency data while correcting biased low frequency information. It was noted that misalignments were causing incorrect AVO inversion results such as small NI values and our workflow corrected those errors.

4.2 Data description and preprocessing

We started processing a surface seismic data set from the Ursa field in the Mississippi Canyon Block 809 (Figure 4.1). With the water depth of about 1300 m, several oil reservoirs (between 5200-6000 m) and a fizz and a oil reservoirs (near 3700 m) can be

Table 4.1. Amplitude and frequency preserving processing flow before AVO analysis. Note that three different demultiple algorithms and velocity update using migration iterations will be used.

Processing sequence	**Objectives**
Trace edit	Fill missing and bad traces
Beam-Streer interpolation	Regularize the dataset from 50 m shot spacing to 25 m
Surface consistent scaling	Correct inconsistent amplitude among shot gathers from acquisition and FX interpolation
Initial velocity analysis	Pick stacking velocity for each CMP gathers
Demultiple	Remove surface related multiples
Prestack time migration	Map reflectors into true subsurface locations and collapse diffractions

found. These reservoirs are located near the salt flank in the form of stacked pinchout reservoirs. With known reservoir information from well logs, our objective here is to analyze two closely spaced reservoirs (one fizz and one oil) using our frequency dependent AVO analysis technique. The preprocessing workflow and the objectives of each step are shown in Table 4.1.

For a successful application of our frequency dependent AVO workflow, we need to preserve amplitude information in addition to frequency content. There are several processing elements that could affect both measurements. For example, the wavelet deconvolution that is routinely applied to seismic data could suppress important low frequency information. Also, a true amplitude recovery (TAR) process that is commonly used to compensate geometrical spreading and average Q effect without any accurate physical basis might harm truthful analysis. Our approach to preserve frequency and amplitude information is to process seismic data without any elements that might affect amplitude and frequency content while applying a model based geometrical spreading correction just before the AVO attribute inversion process.

One of the first problems we faced in our time processing flow was the suppression

of free surface multiples. In a deep water environment, multiples generally have larger moveouts which can be easily handled with moveout-based demultiple algorithms such as the radon demultiple method. We might need a more sophisticated demultiple algorithm to deal with deep water subsalt reservoirs in a future data set, but the radon demultiple algorithm removed a significant amount of multiple energy in this data set (Figure 4.2).

An NMO stacked section after multiple removal is shown in Figure 4.3. There are several issues which need to be resolved. One of the biggest problems was the interference between (1) events from target reservoirs and (2) signals from salt flanks and diffractions. Sophisticated depth migration algorithms, such as Kirchoff, wave equation, and reverse time migration, could resolve this problem with accurate structure information, but not with correct amplitudes due to the difficulty of estimating exact velocity field. One the other hand, prestack time migration is known to preserve amplitude information better and have used for AVO analysis. As noted earlier, our objective here is to process seismic data with the least amount of distortion in amplitude and frequency possible.

Considering the relatively small dip of target events, we migrated data with a processing flow of NMO, FK DMO, FK migration (prestack time equivalent migration). After NMO (Figure 4.3) and DMO processes, events will be moved to zero offset locations. Then using the zero offset migration principle, we can collapse diffractions and move events to true subsurface location (Figure 4.4).

Figure 4.5 shows a smoothed interval velocity model converted from rms (root mean square) velocity using Dix equation.

Figure 4.6 shows zoomed pictures of the stack after NMO and the stack after prestack time equivalent migration. Note that these are two events from target reservoirs that will be discussed in detail in a later section. Interference among target and salt flank reflections, and diffractions, are well separated and removed after prestack time migration. In individual CMP and CRP gathers, we can see that the ambiguity of dips between reservoir events and steep dip salt flank events were well resolved (Figure 4.7).

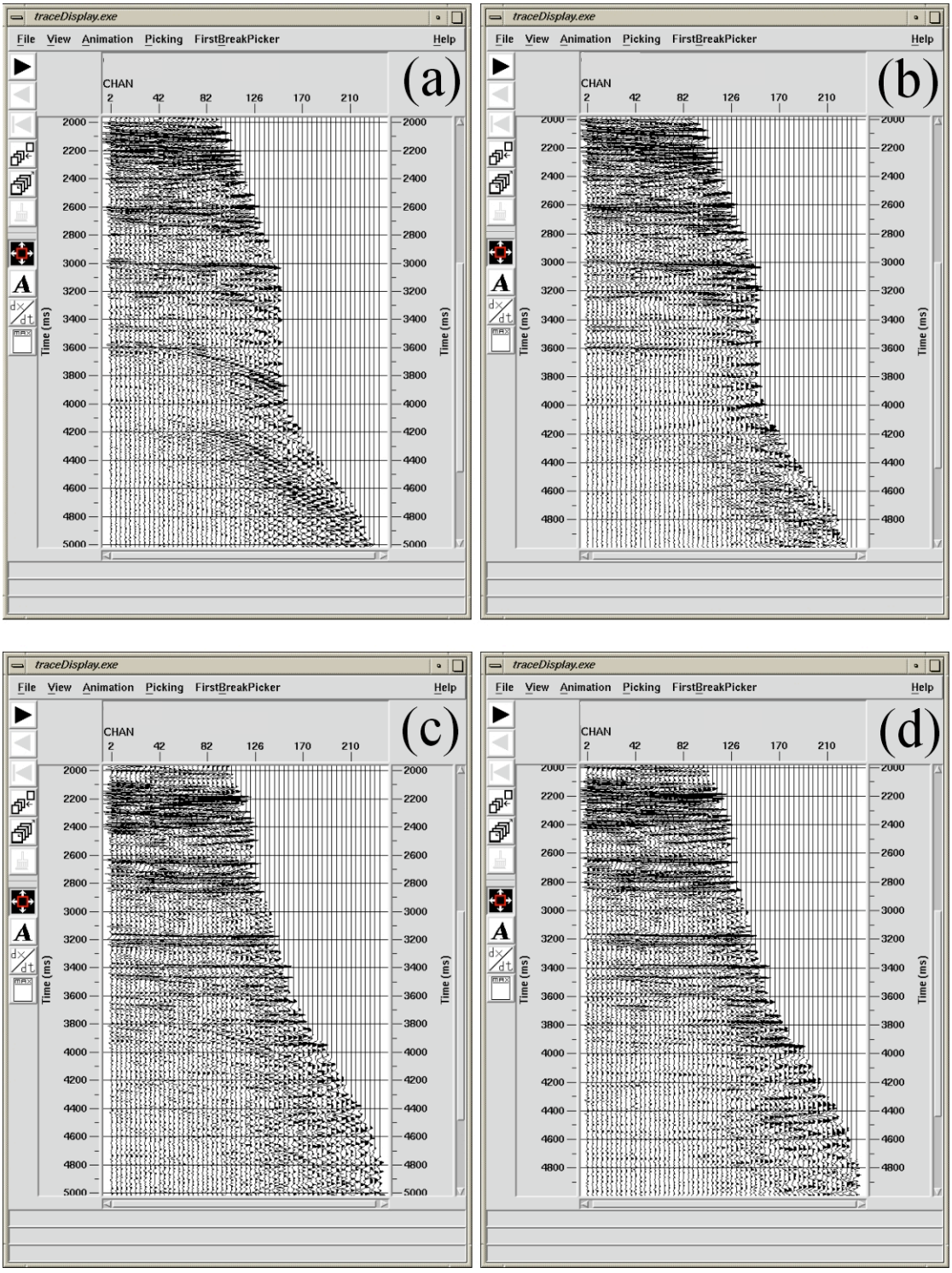

Fig. 4.2. Before and after the radon demultiple of two CMP gathers near target reservoirs. (a) and (b): before and after at the first CMP. (c) and (d): before and after at the second CMP. Free surface multiples interfere with relatively weaker primaries from target reservoirs at 4.2 s. Relatively stronger far offset signals were coming from salt flanks resulting in ambiguity in velocity picking.

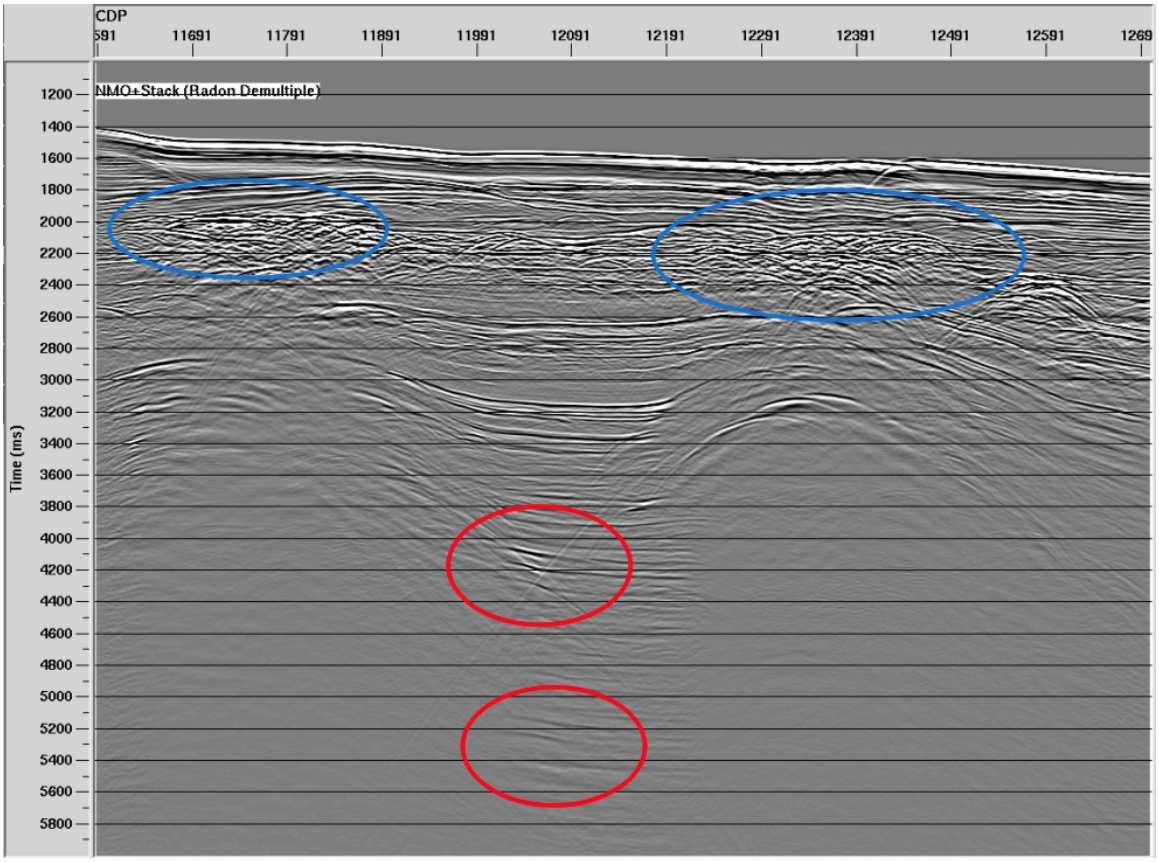

Fig. 4.3. NMO+stack. Blue ovals represent channel margin slumping on top of salt bodies and the red ovals are the location of target reservoirs. Note that no scaling (i.e. geometrical spreading or Q compensation) has been applied yet. Each plot was normalized to its global maximum (correct relative amplitude).

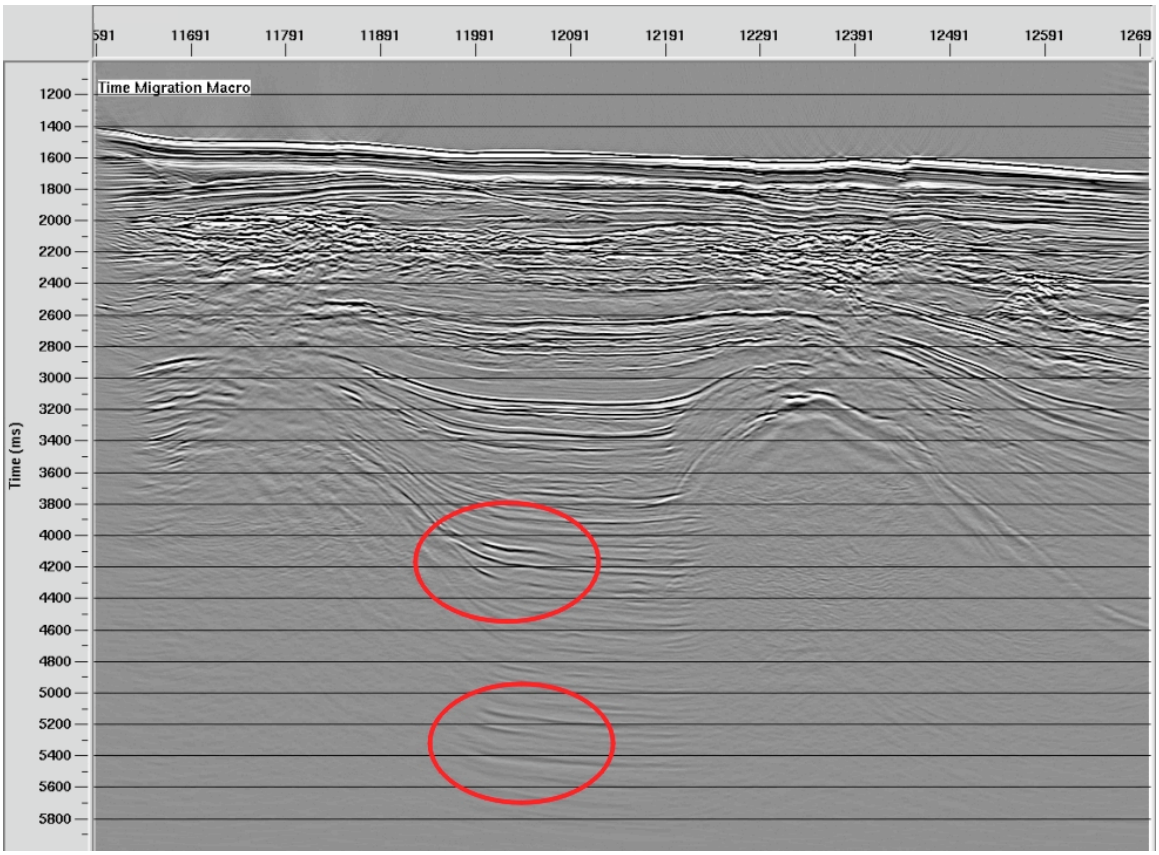

Fig. 4.4. PSTM+stack. Red ovals are the location of target reservoirs. Note that no scaling (i.e. geometrical spreading or Q compensation) has been applied yet. Each plot was normalized to its global maximum (correct relative amplitude). Note that after migration, target reservoirs moved into up-dip direction while many diffractions especially near channel margin slumping were collapsed. Also, synclines between two salt bodies were widened while anticlines at the top of each salt were narrowed.

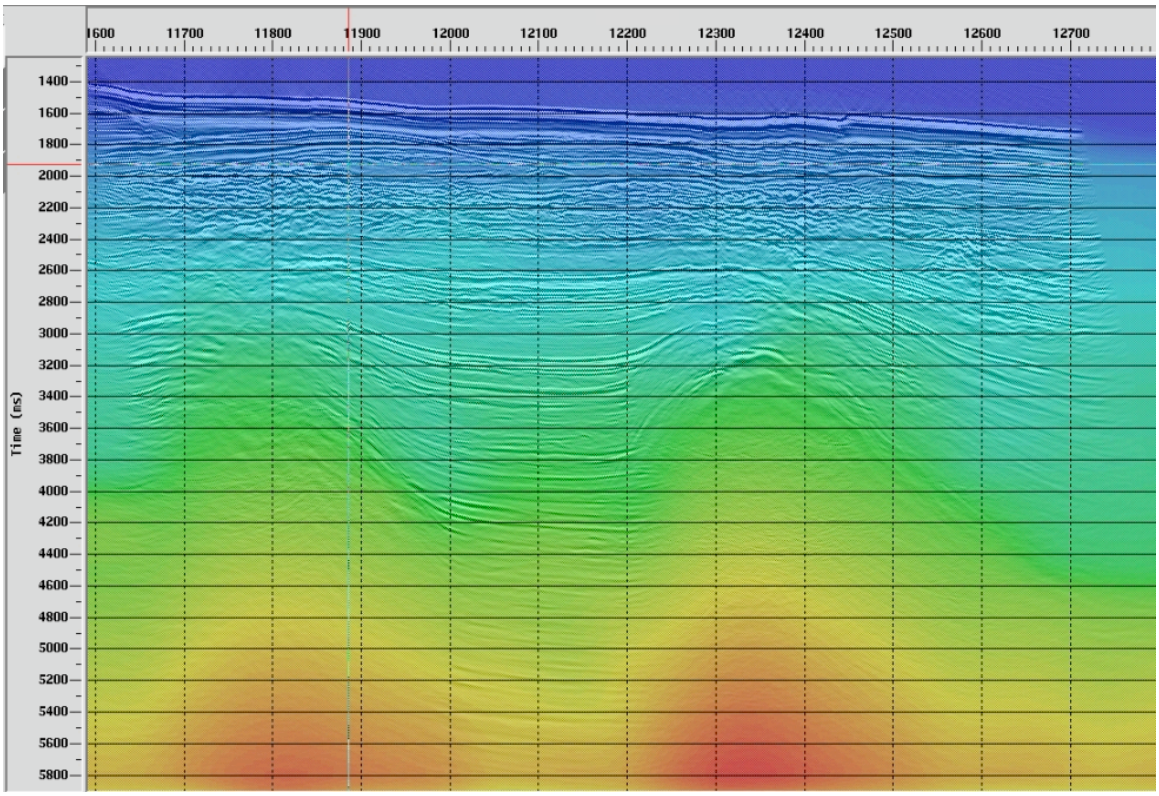

Fig. 4.5. Interval velocity overlay with migrated section after one iteration.

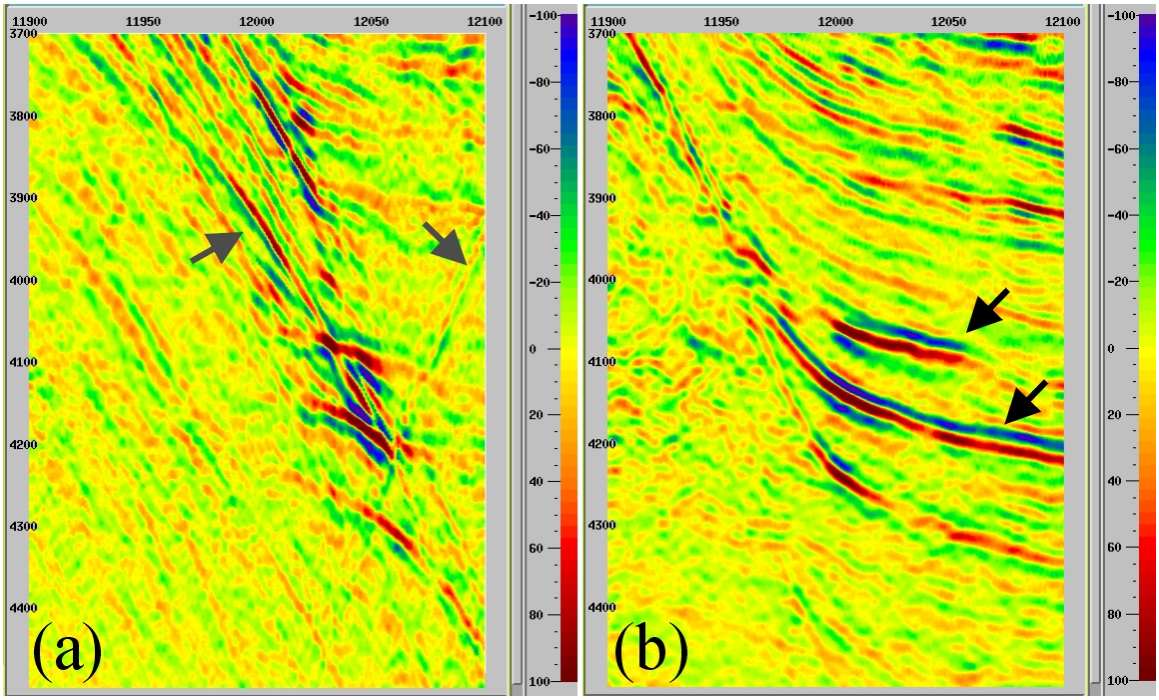

Fig. 4.6. Zoomed picture of (a) NMO and (b) PSTM stacks. The gray arrows in (a) represent signals from salt flanks (left) and top salt diffractions (right). The black arrows in (b) denote signals from two target events (Upper: fizz, lower: oil). Severe interferences among signals were cleared after the prestack time migration.

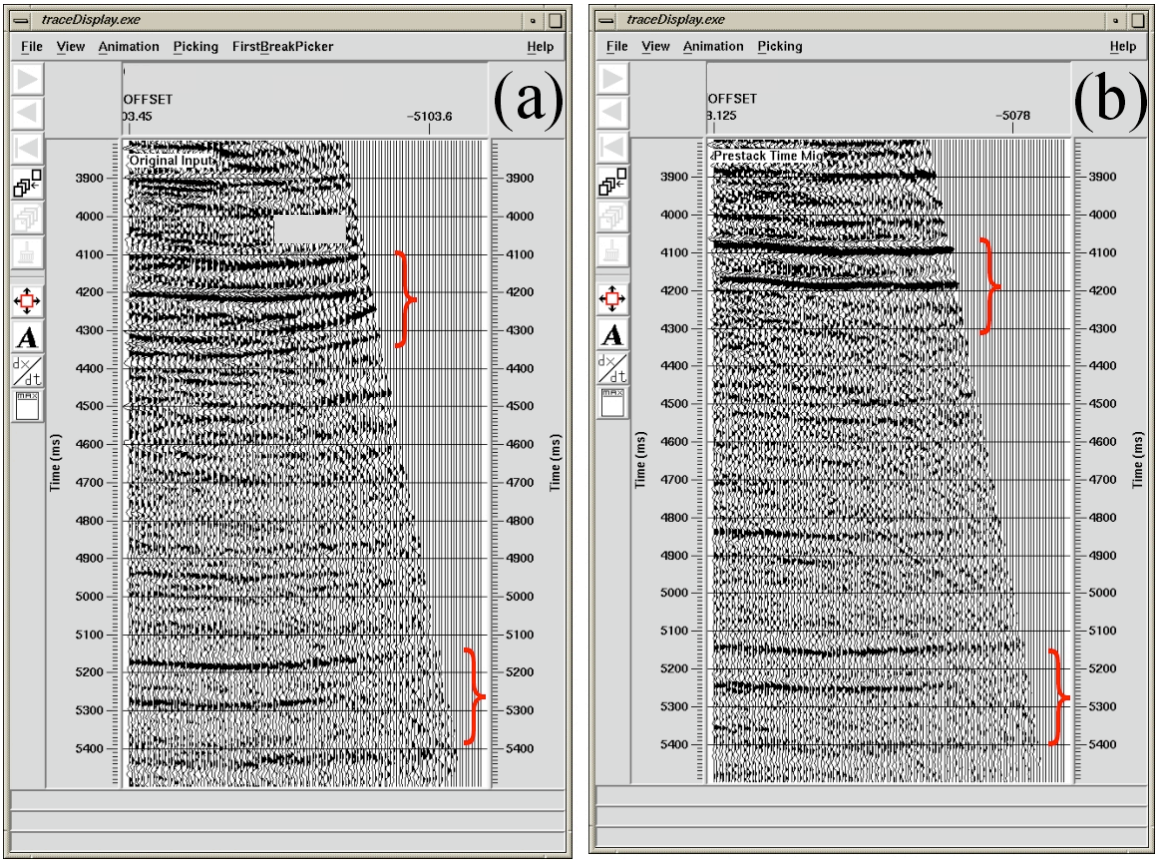

Fig. 4.7. A CMP gather from NMO and a CRP gather from PSTM. Red intervals mark known target reservoirs. Complicated interference was reduced after PSTM.

4.3 Synthetic test of substack scheme

Analysis of field data showed that gathers with low signal-to-noise ratio (S/N) made spectral decomposition and frequency domain AVO very difficult. This was confirmed by tests with synthetic seismograms, tests that also allowed the development of a processing step to improve results. An effective solution is to substack four adjacent input traces prior to the stretch correction. The tradeoff could be possibly losing frequency information, so we extensively tested our substack scheme on synthetics with different S/N ratios. We used a simple thin layer model using P- and S-wave velocities and densities from well log. Noise free data and S/N ratios of 2, 5, 10 have been tested. Fig 4.8 shows synthetic seismograms before stretch correction (a and d), after-substack only (b and e), and after-substack and stretch correction (c and f). The initial data have 25 m receive spacing, and the after-substack gather has 100 m. Note that only traces located every 100 m in offset were plotted in the first row to simplify comparisons. The substack process shows significant improvement in data quality. But, the wide wavelet from NMO stretch distortion is still observable at far offset traces. This has been corrected after-substack and stretch correction process (Fig 4.8 c and e). Fig 4.9a shows crossplots from noise free case. No measurable differences exist between raw input data (correct answer) and the substack, while the stretch correction reduces variation in attributes. In the S/N=2 case (Fig 4.9b), more variation exists in raw and substacked cases while the combination of substack with stretch correction processes constrained data points within acceptable ranges, which was similar to that from noise free data. Note that some other outliers from input and substack only case are not shown to simplify comparisons.

4.4 Ursa, deep water GOM example

Our new frequency dependent AVO analysis workflow with the substack scheme to increase S/N ratio has been applied to a deep water, GOM data set. We carefully chose preprocessing elements to preserve amplitude and frequency information. Fig 4.10a shows a CRP gather for our two target reservoirs that were previously shown in Figure 4.6. The NMO stretch is clearly visible at far offset traces, while the new substack procedure combined with the stretch correction, compressed the wavelet. Also, the alignment of events has been improved significantly resulting in more accurate AVO

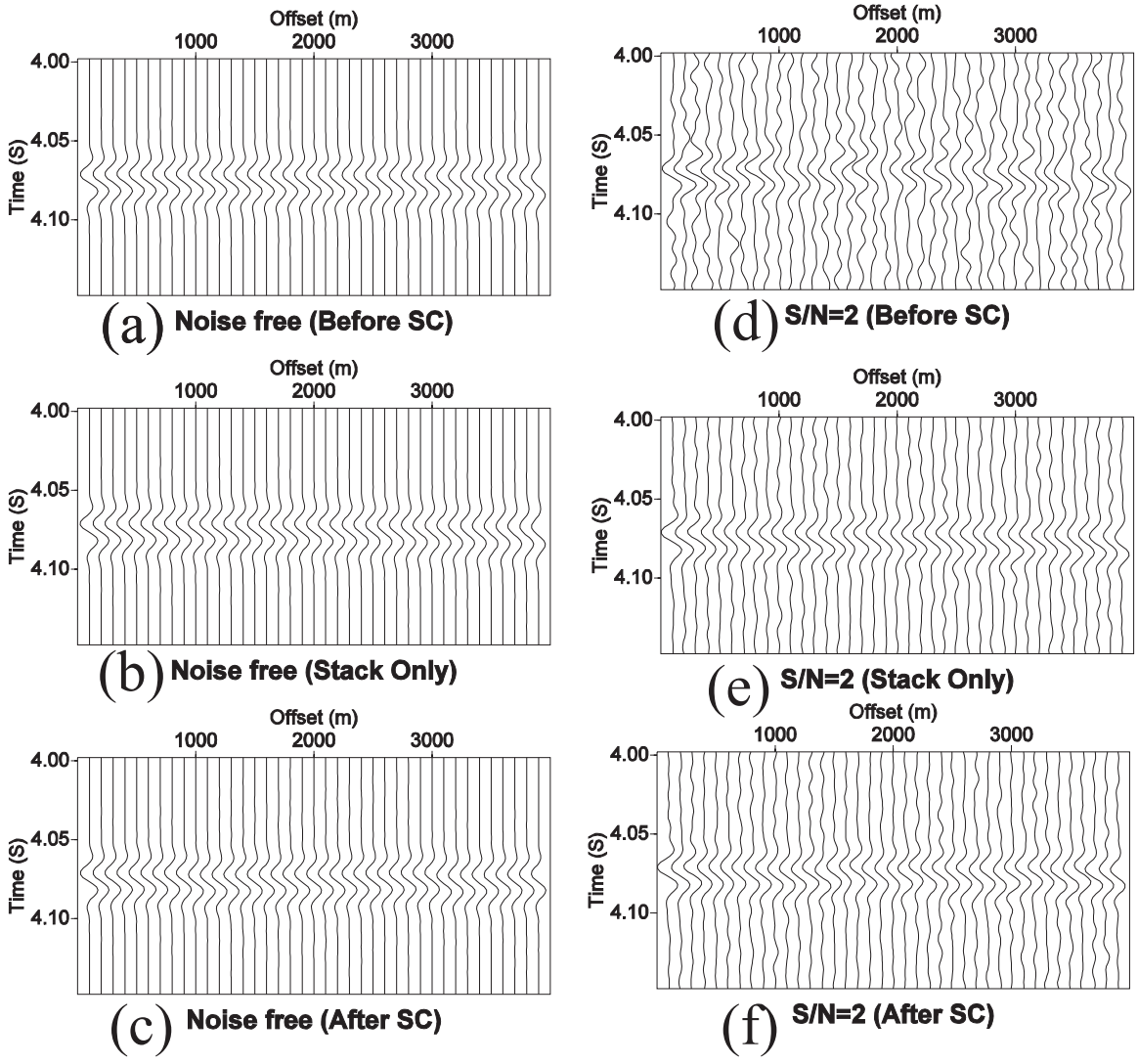

Fig. 4.8. Synthetic seismograms for substack test and stretch correction. Note that only fourth traces (100 m) in the input traces were plotted in (a) and (d).

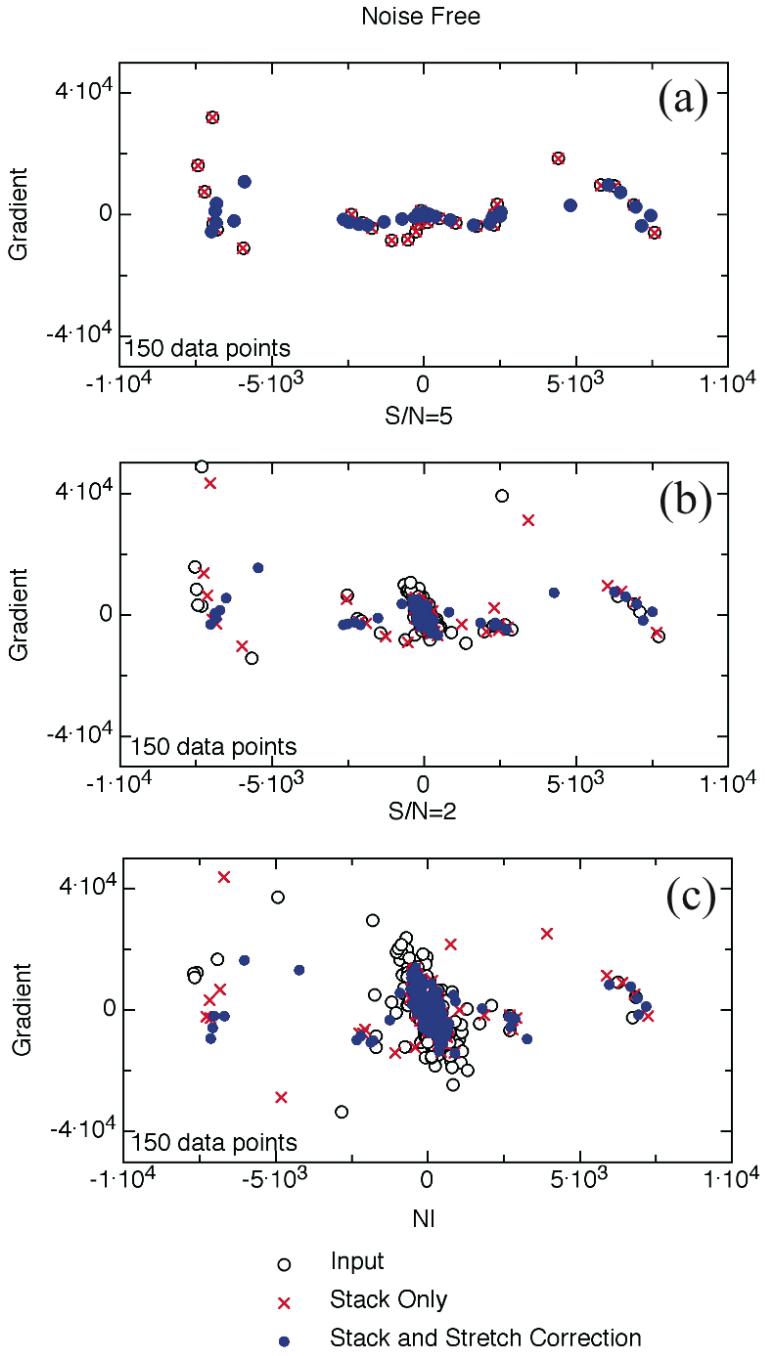

Fig. 4.9. Crossplots of NI and gradient with different S/N ratio. In each plot, three cases of raw input data, substack only, and substack followed by stretch correction are used to invert for attributes. Notice well constrained values from substack followed by stretch correction (blue dots) while severe outliers are clear in substack only case with increasing noise level.

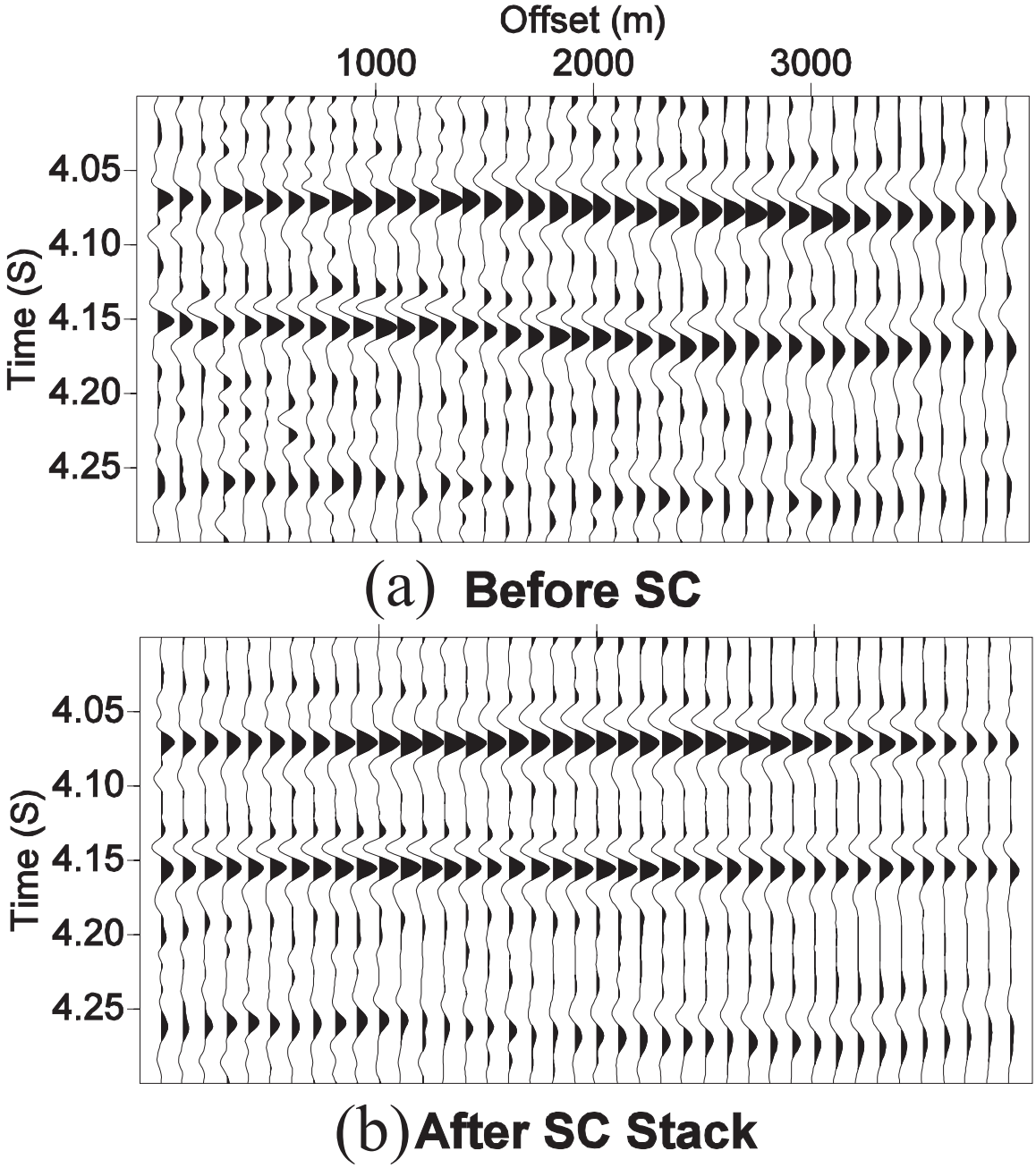

Fig. 4.10. Two GOM deep-water CRP gathers (a) before stretch correction and (b) after stretch correction and stack. Note the increased S/N ratio in addition to improved alignment of events resulting in more accurate AVO inversion result

inversion results. It is hard to see any coherent events in high frequency data before stretch correction in the spectral decomposition display (compare 50 Hz section in Fig 4.11 (a) and (b)). After stretch correction, the large amplitudes at far offset in low frequency data have been reduced, while the very weak amplitude in high frequency data has been enhanced. Also, changes of amplitude become much smoother due to the substack scheme that increased the S/N ratio.

Crossplots of two frequency slices over 20 CMP gathers show us significant improvement in our final output (Fig 4.12). The biased strong low frequency anomaly has been corrected, while background trend only from high frequency data before stretch correction changed into more accurate attribute information after the stretch correction. We can see that the crossplot in Fig 4.12a can be easily interpreted as showing very strong low frequency effects. Also, misalignments cause insignificant crossplots in high frequency data, which is important to compute ratios with respect to low frequency data. In this data, the reservoir thicknesses are 15 and 6 m, which is relatively very thin compared with wavelength (80 m assuming central frequency of 30 Hz and 2500 m/s velocity). We think this is the reason why we see more anomalies in high frequency data, while showing virtually no anomalies in low frequency data. Also the top reservoir was narrow enough so that some rays do not pass the upper reservoir showing almost negligible upper layer effect as we saw in the synthetics from Chapter II.

We only corrected processing artifacts based on the accurate equation that computes the stretch ratio from application of NMO. Though theses changes are significant, this correction will not affect any frequency-dependent effects caused by other by other physical processes such as tuning and attenuation. This will enable us to further study those two important frequency dependent factors which might lead us to any saturation information.

4.5 Conclusions

After careful preprocessing, radon demultiple, and prestack time equivalent imaging, we applied the frequency dependent workflow to a deep water, GOM data set. Unlike unequally spaced CMP gathers in Teal South data set, equally spaced traces after FK DMO allowed us to add a substack scheme which improved S/N ratio significantly. Two target reservoirs were further inverted for AVO attribute analysis after spec-

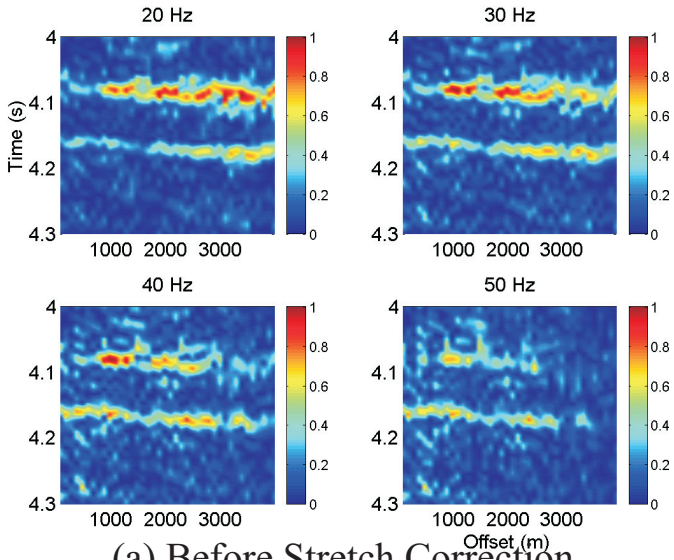

(a) Before Stretch Correction

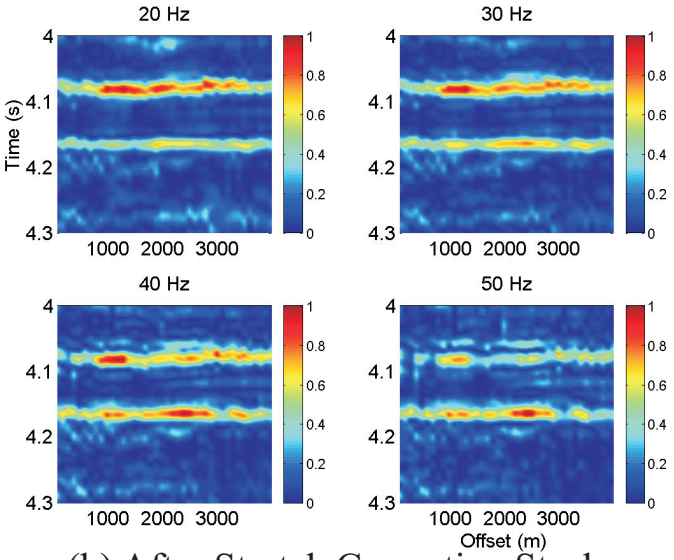

(b) After Stretch Correction Stack

Fig. 4.11. Spectral decomposed prestack gathers (a) before stretch correction and (b) after stretch correction. Each CRP gathers show four frequency slices: 20, 30, 40, 50 Hz. Notice the reduction of the far offset amplitude at 20 Hz and increase of overall amplitude at 50 Hz after stretch correction and stack.

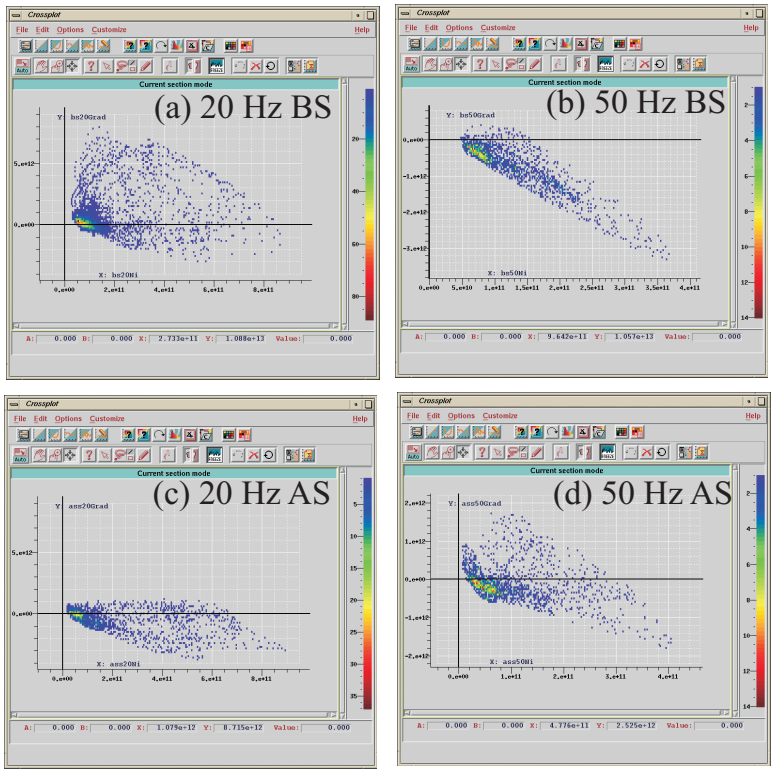

Fig. 4.12. Crossplots of NI and gradient (a) before stretch correction at 20 Hz, (b) before stretch correction at 50 Hz, (c) after stretch correction at 20 Hz, (d) after stretch correction at 50 Hz. At 20 Hz, false anomaly has been moved to the correction positions, while corrected anomalies show up at 50 Hz. BS: Before Stretch correction, AS: After stretch correction.

tral decomposition. AVO crossplots showed that our workflow corrected biased low freuqency data due to NMO stretch while recovering important high frequency information. After the stretch correction, any anomaly in crossplots can be interpreted in terms of two other frequency related effects which are tuning and attenuation. Unlike Teal South data where we observed similar crossplots across frequency, comparing crossplots from low and high frequency data at 20 and 50 Hz of Ursa, we could observe clear frequency dependent AVO effects. Due to the relatively thin layer thickness, crossplots from low frequency data did not show any strong anomaly while those from high frequency data showed very strong anomaly mainly contributed to tuning effect.

CHAPTER V

CONCLUSION

For more accurate amplitude and frequency analysis, an NMO stretch correction scheme based on simple frequency shift was applied to synthetics and several reflections of our interest in the Teal South data. Our current algorithm can be considered as a quick fix for the amplitude based analysis among targets, but it seems to be more effective than wavelet deconvolution based methods that could change the frequency content.

Amplitude and frequency corrections have been verified through full waveform synthetics over wide offsets with the additional improvements of event alignments. Combined with spectral decomposition and AVO attribute analysis toolbox, this workflow was found to be a very fast and effective.

Despite of suboptimal data condition, the field data application to Teal South, GOM clearly showed changes in amplitudes with offset, which result in the increase of gradient attributes significantly in the mid and high frequency regions on Class III AVO anomalies. With more accurate data and improved sensitivity, we should be able to further quantify any frequency changes from different rock or fluid properties.

The substack scheme after the stretch correction reduced significantly the uncertainty and computation time in the spectral decomposition step. With more accurate data and improved sensitivity, we should be able to further quantify any frequency changes from different rock or fluid properties especially in 4-D seismic case after a proper prestack equalization.

The primary contributions of this dissertation are as follows:

- We developed a new processing workflow by combining NMO stretch correction, time-frequency representation (spectral decomposition), and conventional AVO analysis. Without reprocessing the whole data again, our workflow can be used on top of existing workflow for further analysis, such as frequency dependent attribute anaysis or risk assessment.

- Unlike other sophisticated NMO stretch correction, our NMO stretch correction which is based on simple frequency shift scheme proved to be very accurate

(only 1-2% error in amplitude). This algorithm is tested over Teal South shallow water data where we observed significant amount of stretch at far offset. Without stretch correction, we might have to mute large amount of traces. Another benifit of this procedure was the alignment of events based on crosscorrelation. Our AVO inversion tool box performs attribute inversion over contant time slices. Without a proper alignment, we can not get accurate inverted parameters. slices

- We enhanced our algorithm by implementing a substack scheme. Benifits are two fold:more accurate time-frequency representation and faster computation time. It was clearly shown that we will get error-prone inverted attributes which is likely to lead us to wrong interpretation.

- After correct amplitude and frequency information, accurate alignment of events, increased S/N ratio, and reduced data size, we applied our enhanced workflow to Ursa, deepwater GOM data. Significant changes in low and high frequency were observed, showing more scattered AVO cross plots in high frequency data.

REFERENCES

Aki, K., and Richards, P., 1980, Quantitative seismology; theory and methods: W. H. Freeman and Co.

Andre, R., and Rinehart, K. R., 1997, Teal South prospect, offshore Louisiana: Successful redevelopment of abandoned oil field using new technologies: AAPG Ann. Mtg., AAPG, A4.

Batzle, M., Hofmann, R. B., Han, D.-H., and Castagna, J. P., 2001, Fluid and frequency dependent seismic velocity of rocks: The Leading Edge, **20**, no. 2, 168–171.

Batzle, M., Han, D.-H., and Gibson, L., 2002, Seismic saturation: Technical report, DOE.

Biot, M., 1956, Theory of propagation of elastic waves in a fluid saturated porous solid. i. low frequency range and ii. higher-frequency range: J. Acoust. Soc. Am., **28**, 168–191.

Bishop, K., Keliher, J., Paffenholz, J., Stoughton, D., Michell, S., Ergas, R., and Hadidi, M., 2001, Investigation of vendor demultiple technology for complex subsalt geology: SEG Technical Program Expanded Abstracts, **20**, no. 1, 1273–1276.

Bortfeld, R., 1961, Approximation to the reflection and transmission coefficients of plane longitudinal and transverse waves: Geophys. Prosp., **9**, 485–503.

Burnett, M. D., Castagna, J. P., Mendez-Hernandez, E., Rodriguez, G. Z., Garcia, L. F., Martinez-Vasquez, J. T., Tellez-Aviles, M., and Vila-Villasenor, R., 2003, Application of spectral decomposition to gas basins in Mexico: The Leading Edge, **22**, no. 11, 1130–1134.

Castagna, J. P., Sun, S., and Siegfried, R. W., 2003, Instantaneous spectral analysis: Detection of low-frequency shadows associated with hydrocarbons: The Leading Edge, **22**, no. 2, 120–127.

Castoro, A., White, R., and Thomas, R., 2001, Thin-bed AVO: Compensating for the effects of NMO on reflectivity sequences: Geophysics, **66**, no. 6, 1714–1720.

Chiburis, E. F., 1987, Studies of amplitude versus offset in Saudi Arabia: SEG Technical Program Expanded Abstracts, **6**, no. 1, 614–616.

Dragoset, W. H., and Jericevic, Z., 1998, Some remarks on surface multiple attenuation: Geophysics, **63**, no. 2, 772–789.

Dunkin, J. W., and Levin, F. K., 1973, Effect of normal moveout on a seismic pulse: Geophysics, **38**, no. 4, 635–642.

Dziewonski, A., Bloch, B., and Landisman, C., 1969, A technique for the analysis of transient seismic signals: Bull. Seism. Soc. Am., **44**, 1041–1063.

Ebrom, D., 2004, The low-frequency gas shadow on seismic sections: The Leading Edge, **23**, no. 8, 772.

Foster, D. J., and Mosher, C. C., 1992, Suppression of multiple reflections using the radon transform: Geophysics, **57**, no. 3, 386–395.

Gassaway, G. S., 1984, Effects of shallow reflectors on amplitude versus offset (seismic lithology) analysis: SEG Technical Program Expanded Abstracts, **3**, no. 1, 665–669.

Goloshubin, G., and Daley, T., 2001, Seismic low-frequency effects in gas reservoir monitoring vsp data: Seismic low-frequency effects in gas reservoir monitoring vsp data:, Soc. of Expl. Geophys., 71st Annual International Meeting, 1693–1696.

Goloshubin, G., and Korneev, V., 2000, Seismic low-frequency effects from fluid-saturated reservoir: Seismic low-frequency effects from fluid-saturated reservoir:, Soc. of Expl. Geophys., 70th Annual International Meeting, 1671–1674.

Goloshubin, G., Korneev, V., and Vingalov, V., 2002, Seismic low-frequency effects from oil-saturated reservoir zones: Seismic low-frequency effects from oil-saturated reservoir zones:, Soc. of Expl. Geophys., 72nd Annual International Meeting, 1813–1816.

Gomez, C. T., and Tatham, R. H., 2007, Sensitivity analysis of seismic reflectivity to partial gas saturation: Geophysics, **72**, no. 3, C45–C57.

Han, D.-H., and Batzle, M., 2002, Fizz water and low gas-saturated reservoirs: The Leading Edge, **21**, no. 4, 395–398.

Han, D., and Batzle, M. L., 2005, Diagnosis of "fizz-gas" and gas reservoirs in deep-water environment: Diagnosis of "fizz-gas" and gas reservoirs in deep-water environment:, Soc. of Expl. Geophys., 75th Annual International Meeting, 1327–1330.

Han, D.-H., and Batzle, M. L., 2006, Velocities of deepwater reservoir sands: The Leading Edge, **25**, no. 4, 460–474.

Houck, R. T., 1999, Estimating uncertainty in interpreting seismic indicators: The Leading Edge, **5**, no. 18, 320–325.

Johann, P., Ragagnin, G., and Spinola, M., 2003, Spectral decomposition reveals geological hidden features in the amplitude maps from a deep-water reservoir in the campos basin: Spectral decomposition reveals geological hidden features in the amplitude maps from a deep-water reservoir in the campos basin:, Soc. of Expl. Geophys., 73rd Annual International Meeting, 1740–1743.

Lazaratos, S., and Finn, C., 2004, Deterministic spectral balancing for high-fidelity AVO: SEG Technical Program Expanded Abstracts, **23**, no. 1, 219–223.

Li, Y., Downton, J., and Xu, Y., 2007, Practical aspects of AVO modeling: The Leading Edge, **26**, no. 3, 295–311.

Lin, T. L., and Phair, R., 1993, AVO tuning: SEG Technical Program Expanded Abstracts, **12**, no. 1, 727–730.

Liu, J., Wu, Y., Han, D., and Li, X., 2004, Time-frequency decomposition based on ricker wavelet: SEG Technical Program Expanded Abstracts, **23**, no. 1, 1937–1940.

Liu, E., Chapman, M., Loizou, N., and Li, X., 2006, Applications of spectral decomposition for avo analyses in the west of shetland: SEG Technical Program Expanded Abstracts, **25**, no. 1, 279–283.

O'Brien, J., 2004, Interpreter's corner—seismic amplitudes from low gas saturation sands: The Leading Edge, **23**, no. 12, 1236–1243.

Ostrander, W. J., 1986, Plane-wave reflection coefficients for gas sands at nornnormal angles of incidence: Geophysics, **49**, 1637–1648.

Partyka, G., Gridley, J., and Lopez, J., 1999, Interpretational applications of spectral decomposition in reservoir characterization: The Leading Edge, **18**, no. 3, 353–360.

Pennington, W. D., Acevedo, H., Haataja, J. I., and Minaeva, A., 2001, Seismic time-lapse surprise at teal south: That little neighbor reservoir is leaking!: The Leading Edge, **20**, no. 10, 1172–1175.

Rutherford, S. R., and Williams, R. H., 1989, Amplitude-versus-offset variations in gas sands: Geophysics, **54**, no. 6, 680–688.

Sbar, M. L., 2000, Exploration risk reduction: An AVO analysis in the offshore middle miocene, central Gulf of Mexico: The Leading Edge, , no. 19, 21–27.

Shuey, R. T., 1985, A simplification of the Zoeppritz equations: Geophysics, **50**, 609–614.

Stovas, A., Landro, M., and Avseth, P., 2006, Avo attribute inversion for finely layered reservoirs: Geophysics, **71**, no. 3, C25–C36.

Strudley, A., 1990, Amplitude versus offset: Methodology and application to pore fill prediction in the danish central graben: SEG Technical Program Expanded Abstracts, **9**, no. 1, 1523–1525.

Swan, H. W., 1999, Removal of offset-dependent tuning in avo analysis: Removal of offset-dependent tuning in avo analysis:, Soc. of Expl. Geophys., 69th Annual International Meeting, 175–178.

Verschuur, D. J., Berkhout, A. J., and Wapenaar, C. P. A., 1992, Adaptive surface-related multiple elimination: Geophysics, **57**, no. 09, 1166–1177.

Weglein, A. B., Gasparotto, F. A. F., Carvalho, P. M., and Stolt, R. H., 1997, An inverse-scattering series method for attenuating multiples in seismic reflection data: Geophysics, **62**, no. 06, 1975–1989.

Wrolstad, K. H., 1986, Offset-dependent amplitude analysis by viscoelastic lithological modeling: SEG Technical Program Expanded Abstracts, **5**, no. 1, 341–346.

Zoeppritz, K., 1919, On the reflection and propagation of seismic waves: Gottinger Nachrichten, **I**, 66–84.

VITA

Seung Chul Yoo received a B.S. degree in geology from Korea University (1994), and a M.S. degree in geosciences from Pennsylvania State University (1998). He spent two summers in demultiple research at Phillips Petroleum Company and is now working as a geophysicist at GX Technology. His permanent address is Dept. of Geology and Geophysics. To Dr. Richard Gibson, 3115 Texas A&M University, College Station, TX 77843. and his email address is seungyoo@hotmail.com.

This document was typeset in LaTeX by Seung Chul Yoo.